ApJ Accepted, 2003 April 21

Optical Identification of the *ASCA* Medium Sensitivity Survey in the Northern Sky : Nature of Hard X-ray Selected Luminous AGNs[1]

Masayuki Akiyama

Subaru Telescope, National Astronomical Observatory of Japan, Hilo, HI, 96720

akiyama@subaru.naoj.org

Yoshihiro Ueda

Institute of Space and Astronautical Science, Sagamihara, Kanagawa, 229-8510, Japan

ueda@astro.isas.ac.jp

Kouji Ohta

Department of Astronomy, Kyoto University, Kyoto, 606-8502, Japan

ohta@kusastro.kyoto-u.ac.jp

Tadayuki Takahashi

Institute of Space and Astronautical Science, Sagamihara, Kanagawa, 229-8510, Japan

takahasi@astro.isas.ac.jp

and

Toru Yamada

National Astronomical Observatory of Japan, Mitaka, 181-8588, Japan

yamada@optik.mtk.nao.ac.jp

ABSTRACT

We present the results of optical spectroscopic identifications of a bright subsample of 2–10 keV hard X-ray selected sources from the *ASCA* Medium Sensitivity Survey in the northern sky (AMSSn). The flux limit of the subsample

is 3×10^{-13} ergs s^{-1} cm^{-2} in the 2–10 keV band. All but one of the 87 hard X-ray selected sources are optically identified, with AGNs (including broad-line AGNs, narrow-line AGNs, and 3 BL Lac objects), 7 clusters of galaxies, and 1 galactic star. It is the largest complete sample of hard X-ray selected AGNs at the bright flux limit. Amounts of absorption to their nuclei are estimated to be hydrogen column densities ($N_{\rm H}$) of up to $\sim 3 \times 10^{23}$ cm^{-2} from their X-ray spectra. Optical properties of X-ray absorbed AGNs with $N_{\rm H} > 1 \times 10^{22}$ cm^{-2} indicate the effects of dust absorption: at redshifts, $z < 0.6$, AGNs without broad Hβ emission lines have significantly larger $N_{\rm H}$ value than AGNs with broad Hβ emission lines. At $z > 0.6$, the X-ray absorbed AGNs have a large hard X-ray to optical flux ratio ($\log f_{2-10\ {\rm keV}}/f_R > +1$). However, three X-ray absorbed $z > 0.6$ AGNs show strong broad lines. In combination with hard X-ray selected AGN samples from the *ASCA* Large Sky Survey, the *ASCA* Deep Survey in the Lockman Hole and *Chandra* Deep Field North, the luminosity distributions of absorbed ($N_{\rm H} > 1 \times 10^{22}$ cm^{-2}) and less-absorbed ($N_{\rm H} < 1 \times 10^{22}$ cm^{-2}) AGNs are compared.

Subject headings: diffuse radiation — galaxies: active — quasars: general — surveys — X-rays: diffuse background

1. INTRODUCTION

Revealing the origin of the Cosmic X-ray Background (CXB) is one of key issues in understanding the growth of central massive black holes in galaxies (Barger et al. 2001). Recently, ultra deep >1Ms pointing observations with *Chandra* resolve 80%–90% of the CXB into discrete sources in the 0.5–10 keV energy range (Brandt et al. 2001; Rosati et al. 2002). Preliminary results of optical identifications of these sources suggest that they mostly originate from accretion processes in AGNs, although there are contributions from hot gas of elliptical galaxies and X-ray binaries of starburst galaxies at the faintest flux level (Hornschemeier et al. 2001). Therefore the CXB is thought to be an integrated emission of AGNs with various redshifts, luminosities, and types; in other words, it reflects the cosmic growing process of the central massive black holes in galaxies.

---

[1]Based on data collected at 8.2m Subaru Telescope, which is operated by the National Astronomical Observatory of Japan, University of Hawaii 2.2m telescope, Kitt Peak National Observatory 2.1m telescope, and Calar Alto 3.5m telescope.

A significant fraction of the accretion process is expected to be obscured by absorbing matter in AGNs (Comastri et al. 1995; Gilli et al. 2001). The intensity and the spectrum of the CXB are well modeled if we assume that there are four times more absorbed AGNs than non-absorbed AGNs (Comastri et al. 1995). In the model it is assumed that the fraction of absorbed AGNs in low-luminosity AGNs, i.e. Seyfert galaxies, can be simply extrapolated to high-luminosity AGNs, i.e. QSOs. In the local universe ($z < 0.03$), the number density of narrow-line low-luminosity AGNs (Seyfert 2s) is three times larger than that of Seyfert 1s (Maiolino & Rieke 1995). On the other hand, for high-luminosity QSOs, only several candidates of absorbed narrow-line luminous QSOs have been found in contrast to the fact that several thousands of broad-line QSOs have been cataloged. The model of the CXB expects that there are many absorbed luminous QSOs, which escape from traditional QSO survey methods with optical/UV or soft X-ray selections. However, there is another possibility that the number ratio between absorbed and non-absorbed AGNs depends on intrinsic luminosities of AGNs and it decreases with increasing luminosity. For this case, the CXB can be dominated by absorbed Seyfert galaxies (Franceschini, Braito & Fadda 2002). In order to specify the site (QSOs or Seyferts ?) of the major growth of the central massive black holes of galaxies, it is very important to reveal the number density of absorbed QSOs.

Since hard X-rays can penetrate absorbing materials of AGNs, AGNs with hydrogen column density, $N_{\rm H}$, as large as 1×10^{23} cm^{-2} can be detected without a significant bias, using 2–10 keV hard X-ray emission. Several candidates of high-redshift absorbed QSOs are found in optical spectroscopic identifications of hard X-ray selected sources (e.g. Ohta et al. (1996) with *ASCA*, and Stern et al. (2002) with *Chandra*). Additionally, one third of the optical counterparts of the hard X-ray selected sources in the ultra deep *Chandra* survey have a faint optical magnitude, and most of the faint optical counterparts could be obscured QSOs (Alexander et al. 2001). These discoveries of candidates of obscured QSOs imply that a significant fraction of the QSO population has been missed because of absorption to the nucleus. The fraction of absorbed QSOs in the whole QSO population is not clear. The optical spectroscopic identifications of the faint hard X-ray selected sources are not complete and insufficient to examine the fraction of absorbed QSOs in detail. Nuclear emissions of absorbed QSOs in the optical wave-band are expected to be fainter than those of non-absorbed QSOs due to dust absorption to their nuclei. Since absorbed QSOs are difficult to identify in comparison with non-absorbed QSOs, the limit in magnitude for optical identifications could introduce bias against absorbed QSOs. Therefore, a sample of hard X-ray selected sources with highly complete optical identifications is necessary to estimate the fraction of absorbed QSOs.

In order to construct a sample of hard X-ray selected AGNs, we performed optical identification of 34 hard X-ray-selected sources from the *ASCA* Large Sky Survey (hereafter

ALSS; Ueda et al. 1999a; Akiyama et al. 2000 [AOY00]) which covers 5.4 square degrees with a flux limit of 1×10^{-13} ergs s^{-1} cm^{-2} $(2-10$ keV) with the *ASCA* Solid-state Imaging Spectrometer (SIS; Burke et al. 1991). All but one source are identified with 30 AGNs, 2 clusters of galaxies and 1 galactic star.[2] In the identified AGNs in ALSS, there is no high-redshift luminous cousin of Seyfert 2 galaxies. The redshift distribution of narrow-line AGNs with $N_{\rm H} > 1 \times 10^{22}$ cm^{-2} is limited to $z < 0.5$, in contrast to the existence of 15 broad-line AGNs at $z > 0.5$. The difference of the redshift distributions suggests a deficiency of narrow-line AGNs with $N_{\rm H} > 1 \times 10^{22}$ cm^{-2} and large intrinsic hard X-ray luminosity, $L_{2-10{\rm keV}} > 1 \times 10^{44}$ erg s^{-1}. A part of the high-redshift broad-line AGNs are, perhaps, significantly absorbed only in the X-ray band. However, the number of the hard X-ray selected AGNs is too small, especially for luminous AGNs, to make a definitive conclusion.

To expand the sample of hard X-ray selected AGNs, we conducted an optical identification program of a bright subsample of hard X-ray selected sources in the *ASCA* Medium Sensitivity Survey (AMSS; Ueda et al. 1999b; Ueda et al. 2001 [Paper I]). AMSS is a serendipitous source survey based on the Gas Imaging Spectrometer (GIS; Ohashi et al. 1996) data of *ASCA* pointing observations at high Galactic latitude region. From the catalog, 87 bright hard X-ray selected sources in the northern sky are selected above flux limit of 3×10^{-13} ergs s^{-1} cm^{-2} $(2-10$ keV) for the optical identification (hereafter AMSSn sample). By intensive spectroscopic observations, all but one of the 87 sources have been optically identified.

The flux limits of the ALSS and AMSSn are 2 orders of magnitudes shallower than those of deep *Chandra* and *XMM-Newton* surveys. But, the total area of the *ASCA* surveys is about 70 degree^2, and 3 orders of magnitude larger than deep *Chandra* surveys. Thus, the *ASCA* AGNs cover a different region of the redshift versus luminosity diagram in comparison with the AGNs from the deep surveys, and the *ASCA* AGNs are more suitable for studies of QSOs in the intermediate redshift ($z < 1$) universe (see Section 3.6). Additionally, the brighter hard X-ray selected sources of the *ASCA* surveys with brighter optical counterparts than the deep surveys make it possible to achieve a complete optical identification of hard X-ray selected sources. The *ASCA* AGNs provide us a unique opportunity to examine the fraction of absorbed QSOs in the intermediate redshift universe. The model of the CXB predicts that 40% of the AGNs detected above the flux limit of *ASCA* should be significantly absorbed, and the *ASCA* flux limit is sufficient to detect the tip of the iceberg of the absorbed AGN population which contributes to the CXB (Comastri et al. 1995).

---

[2]Later *Chandra* follow-up observation suggests that the source without an identification (AX J131832+3259) is a fake source (Ueda et al. in preparation). It is consistent with the estimated number of fake sources in the ALSS sample.

Details of the AMSSn sample are described in Section 2. The identifications are summarized in Section 3. From the identified hard X-ray selected sources, natures of hard X-ray selected AGNs are discussed and the fraction of absorbed AGNs in combination with the hard X-ray selected AGNs from ALSS, *ASCA* Deep Survey in the Lockman Hole, and *Chandra* Deep Field North are examined (Section 4). Radio properties of the AMSSn AGNs are discussed in Section 5. Summary is given in Section 6. The hard X-ray luminosity function of the hard X-ray selected AGNs is discussed in a separate paper (Ueda et al. 2003). In this paper, H_0 of 50 km s^{-1} Mpc^{-1} and q_0 of 0.5 are used throughout.

2. SAMPLE

AMSS is a serendipitous source survey based on the 368 combined fields of *ASCA* GIS pointing observations at high Galactic latitude ($|b| > 10°$) observed in the period between 1993 May and 1996 December. In total, 370 sources are extracted from the *ASCA* GIS data above 5σ in the 2–10 keV band serendipitously. In order to concentrate on bright hard X-ray selected sources, for which a position and an X-ray spectrum are determined relatively well, X-ray sources are selected with the criteria: 1) the detection significance in the 2–10 keV band is $> 5.5\sigma$; 2) the Galactic-absorption-corrected countrate in the 2–10 keV band is > 2.7 counts ks^{-1}, which corresponds to 3×10^{-13} ergs s^{-1} cm^{-2} if we assume an X-ray source with a power-law spectrum with a photon index of 1.7 and no absorption; 3) the distance from the center of GIS field of view is $< 20'$; 4) the Galactic latitude is $|b| > 30°$; 5) the declination is $> -20°$; and 6) the source is not a primary target of the *ASCA* observation and is not physically related to the primary target. With these criteria, 87 X-ray sources are selected in the hard X-ray band from the original AMSS catalog. They are listed in Table 1 with the significance in the hard X-ray band (σ) and the X-ray coordinate. For convenience, each X-ray source is referred to as its exact name and identification number, like 1AXG J000605+2031(NE01). Galactic-absorption-corrected count rates of the sources in the hard and soft X-ray bands are listed in the "Count rate" column in Table 2. The Galactic hydrogen column density estimated from HI observations (Dickey & Lockman 1990) is used ("$N_{\rm H}$" in Table 2). The total survey area depends on the count rate limit: for example, 34 degree^2 and 68 degree^2 with the count rate limits of 2.7 counts ks^{-1} and 10 counts ks^{-1} in the 2–10 keV band, respectively (for the survey area as a function of count rate limit, see Ueda et al. 2003). The former and the latter count rate limits correspond to 3×10^{-13} ergs s^{-1} cm^{-2} and 1×10^{-12} ergs s^{-1} cm^{-2} for a power-law spectrum with a photon index of 1.7 and no absorption, respectively.

A difficulty for the optical identification of the X-ray sources detected by *ASCA* is their

positional uncertainties which are caused by (1) an error of the absolute satellite attitude determination; (2) a combined error caused by source confusion and a statistical fluctuation due to a limited number of photons; and (3) other systematic errors unique to the GIS instruments, such as the position linearization maps, the grid support structure, etc (Paper I). Therefore, for the current identification project, we select X-ray sources which have sufficient counts ($> 5.5\sigma$), such that, at least, the positional uncertainty caused by (2) is suppressed as much as possible. For example, for a source with a high significance (10σ) within $15'$ from the GIS field center, the positional uncertainty, i.e., 90% error radius, is $0\farcm94$, and for a source with the lowest sigma (5.5σ) at $20'$ from the GIS center, the total positional uncertainty goes up to $1\farcm58$. The positional uncertainty of each X-ray source is listed in the "Unct." column of Table 1.

For each X-ray source, hardness ratio, $HR \equiv (H-S)/(H+S)$ where H and S represent the countrates corrected for Galactic absorption in the 2–10 keV and 0.7–2 keV bands respectively (columns "H" and "S" in Table 2), is available in Paper I. The hardness ratio of the source can be converted to the *apparent* photon index ($\Gamma_{\rm app}$) of the best-fit power-law model using the response of the GIS instrument. In this paper, the $\Gamma_{\rm app}$ is referred to describe the apparent X-ray spectral property of each source in the 0.7–10 keV band. The determined $\Gamma_{\rm app}$ index is listed in Table 2.

3. OPTICAL IDENTIFICATION

3.1. Selection of Candidates of Optical Counterparts of X-ray Sources

In order to reveal the nature of the hard X-ray sources, it is crucial to perform optical spectroscopic observations of optical counterparts. We selected candidates of optical counterparts of the hard X-ray sources, using databases of extragalactic objects, soft X-ray sources, and radio sources.

Half of the AMSSn hard X-ray selected sources (37/87) have a cataloged AGN or a cluster of galaxies with a redshift within the error circle (details of literature information from NASA/IPAC Extragalactic Database (NED) are summarized in Section 3.3).

For the remaining 50 sources, the Automatic Plate Measuring machine (APM) catalog, which has limiting magnitude of R of 21 mag (McMahon et al. 1992), was used to search for optical counterparts. The catalog is obtained from scans of glass copies of the Palomar Observatory Sky Survey (POSS) plates. From the ALSS results, it is expected that most of the optical counterparts of the X-ray sources with a hard X-ray flux $> 3 \times 10^{-13}$ ergs s^{-1} cm^{-2} are brighter than 20 mag in R-band (Figure 3 of AOY00). The optical counterparts of

most of the AMSSn X-ray sources should be detected in the APM catalog. The $3' \times 3'$ optical images of the AMSSn source positions are shown in left panels of Figure 1. The images are taken from the Digitized POSS plates, acquisition images during spectroscopic observation mentioned below, or R-band images taken with the University of Hawaii 88″ telescope. All images are centered on the AMSSn source positions, except for 1AXG J000605+2031(NE01), for which the center of the image is shifted. Error circles of the AMSSn sources are indicated with a circle centered on the source position. Most of the AMSSn sources have more than 1 APM object in their error circles.

In order to select the most plausible optical counterpart of each AMSSn X-ray source, *ROSAT* serendipitous source catalogs; the first *ROSAT* source catalog of pointed observations with the high resolution imager (HRI), the second *ROSAT* source catalog of pointed observations with the position sensitive proportional counter (PSPC), and *ROSAT* PSPC WGA catalog (White, Giommi & Angelini 1994), from High Energy Astrophysics Science Archive Research Center (HEASARC) are used. Typical positional uncertainties are 10″ for the HRI sources and 30″ for the PSPC sources. AMSSn sources which do not have a very hard X-ray spectrum can be detected in the soft X-ray *ROSAT* surveys. For example, an X-ray source with a 2–10 keV flux of the AMSSn survey limit, 3×10^{-13} ergs s^{-1} cm^{-2}, the 0.5–2 keV flux is expected to be 1.3×10^{-13} ergs s^{-1} cm^{-2} if the photon index of the source is 1.7 without absorption.

Thirty three AMSSn sources, including sources with a cataloged AGN or cluster of galaxies, have a *ROSAT* HRI source within the error radius. The positions of the HRI sources are marked in the left panels of Figure 1 with a 10″ radius circle. Most of the HRI sources have one candidate optical counterpart. The candidate optical counterparts are listed in Table 1 with an indication "RH" in the selection column. In the HRI error circles of two other sources, 1AXG J160118+0844(NO53) and 1AXG J210738−0512(NO17), there is no optical object cataloged in the APM catalog. In both of the error circles, a faint optical object is detected in a deeper image taken during spectroscopic observation. Thus the faint objects are picked up as candidates of the optical counterparts. In the HRI error circles of other two sources (1AXG J131112+3228(NE22) and 1AXG J164045+8233(NE07)), there is no optical object above R of 21 mag. They are already cataloged as clusters of galaxies, and X-ray spectra of the AMSSn sources are soft ($\Gamma_{\rm app} > 2$). The HRI positions may correspond to a centroid of the whole cluster emission from hot gas, thus the positions do not match any particular galaxy.

Additionally, 48 AMSSn sources have *ROSAT* PSPC serendipitous sources within their error circles. The positions of PSPC sources are marked in the left panel of Figure 1 with a 30″ radius circle. APM objects in the PSPC error circles are observed with high priority

in spectroscopic observations. The positions of sources from the *ROSAT* All-Sky Survey (RASS; Voges et al. 1999) are also marked with a 45″ radius circle in the left panel.

For four AMSSn X-ray sources, 1AXG J010952−1252(SE33), 1AXG J111432+4055(NE26), 1AXG J170730+2353(NO24), and 1AXG J233200+1945(NO18), follow-up hard X-ray observations with *Chandra* are conducted (Ueda et al. in preparation), and 6.78σ, 4.15σ, 2.95σ, and 3.80σ sources respectively are detected in the *ASCA* error circles of the sources. The positions of the detected sources are, $01^{\rm h}09^{\rm m}50\overset{\rm s}{.}90, -12^\circ53'22\overset{''}{.}37$, $11^{\rm h}14^{\rm m}31\overset{\rm s}{.}92, +40^\circ56'14\overset{''}{.}41$, $17^{\rm h}07^{\rm m}32\overset{\rm s}{.}10, +23^\circ53'41\overset{''}{.}95$, and $23^{\rm h}31^{\rm m}58\overset{\rm s}{.}90, +19^\circ44'37\overset{''}{.}68$. At the positions of the *Chandra* sources of 1AXG J010952−1252(SE33), 1AXG J111432+4055(NE26) and 1AXG J170730+2353(NO24), there is an optical object. For 1AXG J233200+1945(NO18), no APM object is in the *Chandra* error circle. A faint optical object discovered in an image taken during a spectroscopic observing run is picked up as the optical counterpart. The optical objects are marked with "CH" in the selection column of Table 1, and the positions of *Chandra* sources are marked with triangles in the left panels of Figure 1.

For 1AXG J233200+1945(NO18) and 1AXG J234725+0053(NE23), follow-up spectroscopic observations with *XMM-Newton* are conducted (Ueda et al. in preparation). The position of 1AXG J233200+1945(NO18) which is determined by the *Chandra* observation is confirmed. For 1AXG J234725+0053(NE23), three X-ray sources are detected near the *ASCA* position. The brightest source is more than three times brighter than the other sources, and consistent with the *ASCA* flux. The position of the brightest source is $23^{\rm h}47^{\rm m}21^{\rm s}, +00^\circ54'27''$. The optical object is marked with "XM" in the selection column of Table 1, and the position of the *XMM-Newton* source is marked with a triangle in the finding chart.

Cross-correlation between the AMSSn X-ray sources and radio sources in the NRAO VLA Sky Survey (NVSS; Condon et al. 1998) in the northern sky ($\delta > -40^\circ$) is also examined. NVSS covers the entire area of the AMSSn survey with a flux density limit of 2.3 mJy at 1.4 GHz. The positional uncertainty of an NVSS source is less than 1″ for relatively bright point sources with a flux larger than 15mJy, and goes up to 7″ for the faintest point sources with a flux density of 2.3 mJy (Condon et al. 1998). Figure 2 shows the stacked surface number density distribution of the NVSS radio sources centered on the 87 AMSSn hard X-ray selected sources. There is an excess of radio source number density. Within 1′ from the positions of the 87 AMSSn sources, there are 34 NVSS radio sources detected. From the number density of radio sources radius between 1′ and 3′, the expected number of contaminating radio sources which are not related to an X-ray source is estimated to be 5.1 ± 0.8 for the 34 radio sources. Therefore at least 85% of the radio sources detected within 1′ from an X-ray source position are likely to be physically related to the X-ray source. The

radio object might be interacting with the X-ray object, and the radio object itself might not be the origin of the X-ray source. The optical counterparts of the radio sources are targets of optical spectroscopy with high priority. The selected objects are indicated with "N" in the selection column of Table 1 and the positions of the NVSS radio sources are marked with large squares in the left panels of Figure 1. Faint Images of the Radio Sky at Twenty-centimeters catalog of radio sources (FIRST; Becker, White, & Helfand 1995) is also used. The survey covers only a part of the AMSSn survey areas with a flux limit of 1mJy (5σ). The positional uncertainty of the FIRST sources is about $1''$ for a point source. The positions of the radio sources are indicated with small squares in the left panels of Figure 1, and an optical counterpart of a FIRST source is marked with "F" in Table 1.

The candidates of optical counterparts selected by the above methods are listed in Table 1. In Figure 1, the listed objects are marked with numbers which indicate identification numbers in APM finding charts. For AMSSn sources which have no information from other catalogs, the brightest and the bluest object in the error circles is observed with high priority.

3.2. Spectroscopic Observations

According to the list of the candidates of optical counterparts, we performed the spectroscopic observations for all sources of our samples, except for candidates of clusters of galaxies. We also obtained optical spectra for sources whose type and redshift were previously known, in order to examine the strength of any emission lines. Most of the spectroscopic observations were conducted with the University of Hawaii $88''$ telescope and KPNO 2.1m telescope. Calar Alto 3.5m telescope and 8.2m Subaru telescope were used for others.

The UH$88''$ observations were made on 2000 March 24, 25, 26, and 27, 2000 October 4, 5, and 6, and 2001 March 19, 20, and 21 with the Wide Field Grism Spectrograph. A grating of 420 grooves mm^{-1} with blaze wavelength of 6400Å was used. The spatial resolution was $0''\!.35$ pixel^{-1} and the typical image size during the observations was $0''\!.8 \sim 1''\!.2$. A slit width of $1''\!.2$ was used. The spectral sampling was 3.75Å pixel^{-1}. The wavelength range from 4000Å to 9000Å was covered without an order cut filter. Obtained spectra were affected by the second-order component above 8000Å. The spectral resolution, which was measured by the HgAr lines in comparison frames and night-sky lines in the object frames, was 12Å (FWHM). For the flux calibration of the data, Feige 34 and BD+28 were observed for spring- and autumn-run, respectively. The same setup including slit width for the objects is used for the standard stars. Imaging data of each X-ray source are taken without a filter for finding charts.

The KPNO 2.1m observations were made on 2000 March 8 and 9 and 2000 October 20, 21, and 22 with the Gold Camera Spectrograph. A grating (#32) with 300 grooves mm^{-1} and a blaze wavelength of 6750Å was used. The spectral sampling was 2.47 Å pixel^{-1}. The wavelength range from 4000Å to 8000Å was covered with an order cut filter for the wavelength range shorter than 4000Å (GG400). The spectral resolution was measured to be 8 Å (FWHM) from night-sky lines in the object frames. The spatial sampling was $0\farcs78$ pixel^{-1}. The typical image size during the observation was $2''$. The slit width was $2''$ for objects. Feige 34 and BD+28 were observed as standard stars in the March and October runs, respectively. The slit width of $10''$ was used for the standard stars to collect its whole light. The other setups are the same for the objects.

Three sources (1AXG J144109+3520(NO32), 1AXG J144301+5208(NO26), and 1AXG J150430+4741(NO12) were observed with the 3.5m telescope at Calar Alto observatory on 1999 April 7 with the MOSCA instrument in a single-slit mode. The g250 grating which has 250 grooves mm^{-1} and a blaze wavelength of 5700Å was used. The spectral coverage ranged from 4000Å to 8000Å. In the configuration, the spectral sampling was 5.95Å pixel^{-1}. A slit width of $1\farcs5$, which was the same as the FWHM of the image size, was used. The spectral resolution was measured to be 24Å (FWHM) from widths of night sky lines in the object frames. The spatial sampling was $0\farcs32$ pixel^{-1}. HD84937 was observed as a standard star with the same setup for the objects.

Two faint objects (1AXG J233200+1945(NO18) and 1AXG J010952−1252(SE33)), were observed on the 8.2m Subaru telescope with the Faint Object Camera And Spectrograph (FOCAS; Kashikawa et al. 2002) on 2001 July 18. A 300 grooves mm^{-1} grating with a blaze wavelength of 5500Å (300B) and an order cut filter below 4700Å (SY47) were used. The spectral sampling was 2.8Å bin^{-1} with 2 pixel binning. The spatial sampling was $0\farcs3$ bin^{-1} with 3 pixel binning. Wavelength range from 4700Å to 9000Å was covered. The slit width was $0\farcs6$ and the image size during the observation was $0\farcs7$. The spectral resolution was measured to be 11Å (FWHM) from night sky lines in the object frames. For the flux calibration, HZ44 was observed as a standard star with a $2''$ slit to collect its whole light.

In order to obtain an optical spectrum with a high signal to noise ratio for the hardest X-ray source 1AXG J170730+2353(NO24), the optical counterpart was observed on the Subaru telescope with FOCAS on 2002 June 7. The slit width of $0\farcs8$ was used and the spatial sampling was $0\farcs4$ bin^{-1} with 4 pixel binning in the spatial direction. All other settings were the same as the previous observation. The image size during the observation was $0\farcs6$. The spectral resolution was measured to be 9.5Å (FWHM) from night sky lines in the object frames. Although the slit width of the observation is larger than the previous observing run, the spectral resolution is higher, probably due to better focusing of spectrograph during the

later observing run. For the flux calibration, HZ44 was observed as a standard star with a $2''$ slit.

The exposure time for each object is indicated at the top of each spectrum in Figure 1.

All of the data are analyzed using IRAF[3]. After bias subtraction, flat-fielding, and wavelength calibration, the optimum extraction method by **apextract** package is used to extract one dimensional spectral data from the two dimensional original data. For the UH data, flux calibrations do not work well for wavelengths > 8000Å, because the spectra of the objects, especially for blue AGNs, and the standard stars are seriously affected by the second order spectra. Using the R magnitude of each object, we estimated the uncertainty of the flux calibration to be factor of 1.7.

3.3. Notes on Individual Identification

The results of the spectroscopic observations are summarized in "Classification" and "Redshift" columns of Table 1. Notes on an individual identification are summarized below. The $10'' \times 10''$ close-up views and the optical spectra of the identified objects are shown in the middle and right panels of Figure 1, respectively. Apparent and absolute properties of the identified objects in the X-ray, optical, near-infrared, and radio wavelengths are summarized in Tables 2 and 3, respectively.

1AXG J000605+2031(NE01) — There is a *ROSAT* PSPC source just outside of the error circle of the AMSSn source. There are 2 bright objects (16_04 and 14_05) in the PSPC error circle. 16_04 is a broad-line AGN at $z = 0.385$ (Giommi et al. 1991; EXO0430.5-1252). 14_05 is a K5-type star. If 16_04 is an X-ray source, the optical-to-X-ray flux ratio, $\log f_{2-10\ \mathrm{keV}}/f_{\mathrm{R}} = -0.22$ is in the range of other AGNs (Figure 6). If this X-ray source originates from a K-type star, we expect that the star has R-band magnitude of 5.0 to 11.2 mag, based on the soft band flux of this source ($f_{0.3-3.5\ \mathrm{keV}} = 1.2 \times 10^{-12}$ erg s^{-1} cm^{-2} from soft band count rate and Γ_{app}), typical optical-to-X-ray flux ratio of K-type stars ($\log f_{0.3-3.5\ \mathrm{keV}}/f_{\mathrm{V}} = -4.0$ to -1.5 from Stocke et al. (1991)), and $V - R$ of 0.9 mag (Pickles 1998). The R-band magnitude of 14_05 is fainter than the expected magnitude range. Therefore, 16_04 is the most plausible optical counterpart of the X-ray source.

[3]IRAF is distributed by the National Optical Astronomy Observatories, which is operated by the Association of Universities for Research in Astronomy, Inc. (AURA) under cooperative agreement with the National Science Foundation.

1AXG J000927−0438(NO19) — There is a *ROSAT* PSPC source detected in the error circle of the AMSSn source. 12_01 is the brightest object in the PSPC error circle. It is identified with a broad-line AGN at $z = 0.314$.

1AXG J001913+1556(NE18) — There is a *ROSAT* PSPC source detected in the error circle of the AMSSn source. There is an NVSS radio source detected at the edge of the PSPC error circle. Optical counterpart of the NVSS source (08_02) is a broad-line AGN at $z = 2.270$ (Marshall et al. 1983; ISS35).

1AXG J002619+1050(NO49) — There is a *ROSAT* HRI source in the error circle of the AMSSn source. Optical counterpart of the HRI source (30_01) is identified with a broad-line AGN at $z = 0.474$.

1AXG J002637+1725(NO50) — There are 2 bright galaxies in the error circle of the X-ray source (19_01 and 20_03). 20_03 is a broad-line AGN at $z = 0.043$, and 19_01 is a companion galaxy with no emission line. The redshift difference of the two galaxies corresponds to a velocity difference of 180 km s^{-1}. There is a faint *ROSAT* HRI source at $1\farcm3$ north from the AMSSn source. With an X-ray spectrum of a power-law with the photon index of 1.7, the expected hard X-ray flux of the HRI source is well below the flux limit of the AMSSn sample, and the *ROSAT* HRI position is well outside of the uncertainty area of the AMSSn source, thus the HRI soft X-ray source is not related to the AMSSn source.

1AXG J010952−1252(SE33) — This source is observed by *Chandra*. The optical counterpart of the *Chandra* source (17_00) shows strong blue continuum with Ca H&K and G-band absorption lines at $z = 0.505$, but without strong emission lines. The optical spectrum is similar to that of a BL Lac object. The object is detected in the NVSS survey, and the radio flux is 3.2mJy. The estimated luminosity $L_{1.4\rm GHz}$ is 3.5×10^{24} W Hz^{-1}, and close to those of radio-loud AGNs in AMSSn sample (see Section 5)

1AXG J015840+0347(NO46) — The brightest object in the error circle of the AMSSn source (17_01) is a broad-line AGN at $z = 0.658$ (Lewis et al. 1979; UM153).

1AXG J023520−0347(NO16) — There is a *ROSAT* PSPC source in the error circle of the AMSSn source. The brightest object in the PSPC error circle (22_01) is a broad-line AGN at $z = 0.376$ (Stocke et al. 1991; MS0232.8−0400).

1AXG J033516−1505(SE20) — There are four optical objects in the error circle of the AMSSn source (16_00, 24_00, 37_02, and 33_01). 37_02 and 33_01 are emission line objects. The former is a narrow-line AGN at $z = 0.122$ and the latter is a narrow-line AGN at $z = 0.501$. For the line ratios diagram, see Figure 4. The AMSSn source is identified with 37_02, because there is a good correlation between hard X-ray flux and [O III]λ5007 line flux

for AGNs (Mulchaey et al. 1994), and the object has 5 times larger [O III]λ5007 flux than 33_01 (Figure 1). 16_00 is a G-type star, and 24_00 is an object without a strong emission line.

1AXG J035008–1149(SE37) — There is a *ROSAT* PSPC source in the error circle of the AMSSn source. The brightest optical object in the PSPC error circle (15_00) is identified with a broad-line AGN at $z = 0.459$. An NVSS source is detected in the error circle of the AMSSn source, but there is no optical counterpart in the error circle of the NVSS source.

1AXG J035137–1204(SE17) — There is a RASS source in the error circle of the AMSSn source. An optical object near to the center of the RASS source (22_02) is identified with a broad-line AGN at $z = 0.182$.

1AXG J041757+0101(NE25) — There is a *ROSAT* PSPC source in the error circle of the AMSSn source. There are two optical objects in the PSPC error circle, and 27_01 is a G-type star and 27_02 is a broad-line AGN at $z = 0.126$. The G-type star is too faint to be the hard X-ray source, and the AMSSn source is identified with the broad-line AGN.

1AXG J043420–0822(NE03) — There is a *ROSAT* HRI source in the error circle of the AMSSn source. An optical object in the error circle (09_01) is identified with a broad-line AGN at $z = 0.154$.

1AXG J044749–0629(NO08) — The brightest object in the AMSSn error circle (10_02) is identified with a broad-line AGN at $z = 0.213$.

1AXG J083747+6513(NO06) — There is a *ROSAT* PSPC source detected in the error circle of the AMSSn source. In the PSPC error circle, an NVSS radio source is detected. The optical counterpart of the NVSS source (18_01) is a broad-line AGN at $z = 1.105$ (Smith et al. 1976; 3C204).

1AXG J090053+3856(NO54) — There is an NVSS radio source detected in the error circle of the AMSSn source. The optical counterpart of the NVSS source (37_01, the brighter component at the east side) is a narrow-line AGN at $z = 0.229$ (Allington-Smith et al. 1985; 0857+39).

1AXG J090720+1639(NO36) — There is a cluster of galaxies at $z = 0.073$ (Stocke et al. 1991; Abell 0744) in the error circle of the AMSSn source. *ROSAT* sources are detected in and around the cluster of galaxies. The X-ray spectrum of the AMSSn source is soft ($\Gamma_{\rm app} = +2.51 \pm 0.07$), and is consistent with X-ray spectra of clusters of galaxies.

1AXG J102337+1936(NE12) — There is a *ROSAT* HRI source in the error circle of the AMSSn source. The brightest object in the HRI error circle (16_01) is identified with a

broad-line AGN at $z = 0.407$.

1AXG J103934+5330(NO11) — There is a *ROSAT* HRI source in the error circle of the AMSSn source. The brightest object in the HRI error circle (12_01) is identified with a broad-line AGN at $z = 0.229$.

1AXG J104026+2046(NO41) — There is a FIRST radio source detected in the error circle of the AMSSn source. An optical counterpart of the radio source (AA) is an elliptical galaxy at $z = 0.240$ and does not show a strong emission line. A blue object ($B - R = 0.51$) near the radio source (12_01) is identified with a broad-line AGN at $z = 0.467$. The AMSSn source is identified with the broad-line AGN.

1AXG J105722−0351(NE14) — There are two *ROSAT* HRI sources detected in the error circle of the AMSSn source. The southern one is nearer to the center of the AMSSn source and is three times brighter than the other one. An optical object (20_02) in the error circle of the southern HRI source is identified with a broad-line AGN at $z = 0.555$ (Stocke et al. 1991; MS1054.8-0335).

1AXG J111432+4055(NE26) — This source is observed by *Chandra*. The optical counterpart of the *Chandra* source (29_02) is identified with a broad-line AGN at $z = 0.153$.

1AXG J111518+4042(NO56) — There is a *ROSAT* HRI source detected at the edge of the error circle of the AMSSn source. The optical counterpart of the HRI source (19_05) is a broad-line AGN at $z = 0.079$ (Stocke et al. 1991; MS 1112.5+4059).

1AXG J121328+2938(NO28) — There is a *ROSAT* HRI source detected in the error circle of the AMSSn source. In the error circle of the HRI source, there are two optical objects, 24_01 and 26_02. 24_01 is a broad-line AGN at $z = 0.143$ (Appenzeller et al. 1998; RX J1213.4+2938). This hard X-ray source is identified with the broad-line AGN. 26_02 is a companion galaxy with HII-region like narrow emission lines (see Figure 4). The redshift difference of the two galaxies corresponds to the velocity difference of 90 km s^{-1}.

1AXG J121359+1404(NO01) — There is a *ROSAT* PSPC and a FIRST radio source (2.9mJy) detected in the error circle of the AMSSn source. The optical object (15_02) at the center of the *ROSAT* PSPC source is identified with a broad-line AGN at $z = 0.154$. The optical counterpart (20_03) of the FIRST radio source is an elliptical galaxy without strong emission line at the same redshift. The redshift difference of the two galaxies corresponds to the velocity difference of 540 km s^{-1}. The AMSSn source is identified with 15_02.

1AXG J121427+2936(NO27) — There is a *ROSAT* HRI source in the error circle of the AMSSn source. The optical object in the error circle of the HRI source (24_01) is a broad-line AGN at $z = 0.309$ (Appenzeller et al. 1998; RX J1214.4+2936).

1AXG J121752+3006(NE02) — There is a *ROSAT* HRI source in the error circle of the AMSSn source. The optical counterpart of the HRI source (23_01) is an AGN at $z = 0.130$ (Strittmatter et al. 1972). The object shows a strong continuum without any strong emission lines, and is a BL Lac object.

1AXG J121854+2957(NO07) — There is a *ROSAT* PSPC source in the error circle of the AMSSn source. The brightest object in the PSPC error circle (17_01) is a narrow-line AGN at $z = 0.178$. For the line ratio diagnostic of the object, see Figure 4. This AMSSn source is identified with 17_01. It is a very red object ($J - K_S = 2.9$), and is discussed in Section 4.2.3. 08_07 is an elliptical galaxy at the same redshift. 02_00, which is located outside of the finding chart, is another companion galaxy of 17_01 with HII-region like narrow-emission lines (see Figure 4). The redshift difference between 17_01 and 02_00 corresponds to the velocity difference of 1500 km s^{-1}.

(This source is also detected by $Beppo-SAX$, and identified with an AGN at $z = 0.18$ (Fiore et al. 1999). The optical spectrum shown in their paper is that of 17_01, but, the coordinate of the optical counterpart in their list is that of 08_07. The J- and K_S-bands magnitudes listed in Maiolino et al. (2000) are also wrong.)

1AXG J121930+0643(NO44) — There is a *ROSAT* HRI source detected in the error circle of the AMSSn source. The optical counterpart of the HRI source (17_01) is a broad-line AGN at $z = 0.081$ (Stocke et al. 1991; MS1217.0+0700). The spectrum of the object shows strong FeII emission lines around 5000Å in observed frame, and the X-ray spectrum is relatively soft ($\Gamma_{\rm app} = +2.22 \pm 0.10$). These properties are similar to narrow-line Seyfert 1s. But, the FWHMs of broad Hα and Hβ lines (~ 3500 km s^{-1}) are larger than those of narrow-line Seyfert 1s (< 2000 km s^{-1}).

1AXG J121930+7532(NO39) — There is a *ROSAT* HRI source detected at the edge of the error circle of the AMSSn source. The optical counterpart of the HRI source (15_02) is a broad-line AGN at $z = 0.464$ (Stocke et al. 1991; MS 1217.4+7549).

1AXG J122003−0025(NO03) — The brightest optical object in the error circle of the AMSSn source is a broad-line AGN at $z = 0.422$ (Croom et al. 2001; 2QZ J122004.3−002540).

1AXG J122017+0641(NO45) — There is a *ROSAT* HRI source detected in the error circle of the AMSSn source. The optical counterpart of the HRI source (06_01) is a broad-line AGN at $z = 0.287$.

1AXG J122049+7505(NO37) — There is a *ROSAT* HRI source detected in the error circle of the AMSSn source. The optical counterpart of the HRI source (21_01) is a broad-line AGN at $z = 0.650$ (Stocke et al. 1991; MS1218.7+7522).

1AXG J122135+7518(NO38) — There is a *ROSAT* HRI source detected in the error circle of the AMSSn source. The optical counterpart of the HRI source (24_01) is a broad-line AGN at $z = 0.073$ (Arakelian et al. 1970; Mrk205).

1AXG J122155+7525(NO40) — There is a cluster of galaxies at $z = 0.24$ (Stocke et al. 1991; MS1219.9+7542) in the error circle of the AMSSn source. There is a *ROSAT* HRI source detected just outside of the error circle of the AMSSn source. The optical counterpart of the HRI source (24_03) shows narrow-emission lines with AGN-like line ratios (see Figure 4). The X-ray spectrum of the AMSSn source is too hard ($\Gamma_{\rm app} = +1.69 \pm 0.23$) to be a cluster of galaxies, thus the AMSSn source is identified with the narrow line AGN at $z = 0.239$.

1AXG J122645−0037(NE05) — There is an NVSS radio source detected in the error circle of the AMSSn source. The optical counterpart of the radio source is an elliptical galaxy at $z = 0.16$. Considering that the X-ray spectrum of the AMSSn source is soft ($\Gamma_{\rm app} = +2.44 \pm 0.20$) and there is a weak excess of faint galaxies around the elliptical galaxy, the AMSSn source is identified with a cluster of galaxies at $z = 0.16$.

1AXG J123605+2613(NE04) — There are a *ROSAT* PSPC source and a FIRST radio source in the error circle of the AMSSn source. The optical counterpart of the FIRST radio source (11_00) shows strong [O III]$\lambda\lambda$5007,4959 and [O II]λ3727 emission lines. Its [O III]λ5007 to Hβ flux ratio is large and consistent with those of Seyfert 2 galaxies. The object is identified with an narrow-line AGN at $z = 0.459$.

1AXG J125732+3543(NO31) — There is a *ROSAT* PSPC source detected in the error circle of the AMSSn source. A blue object (15_01; $B - R = 0.36$) detected in the error circle of the PSPC source is a broad-line AGN at $z = 0.524$ (Marshall et al. 1983).

1AXG J125812+3519(NE16) — There is a *ROSAT* HRI source detected in the error circle of the AMSSn source. The optical counterpart of the HRI source (12_01) is identified with a broad-line AGN at $z = 0.310$. It is originally identified with an AGN at $z = 2.04$ by Weedman (1985) (WEE83). MgII emission line at $z = 0.310$ seems to be mis-identified with Lyα. A strong broad Hα emission line may originate from uncertainty of flux calibration above 8000Å.

1AXG J125828+3528(NE15) — There is a *ROSAT* PSPC source detected in the error circle of the AMSSn source. A FIRST radio source is in the error circle of the PSPC source. The optical counterpart of the FIRST radio source (14_02) is a broad-line AGN at $z = 1.900$ (Braccesi, Lynds, & Sandage 1968; B194).

1AXG J130407+3533(NO30) — There is no optical object in the error circle of the

AMSSn source. Just outside of the error circle, a RASS source is detected. The brightest object in the error circle of the RASS source is a broad-line AGN at $z = 0.329$ (Marshall et al. 1983)

1AXG J130453+3548(NO29) — There are two bright optical objects (26_02 and 22_04) in the error circle of the AMSSn source. 26_02 shows narrow emission lines with HII region like line ratio at $z = 0.034$ (see Figure 4). 22_04 is a Galactic G-star. An optical object just outside of the AMSSn error circle (20_01) is a broad-line AGN at $z = 0.316$. We identified this source with 20_01.

1AXG J131112+3228(NE22) — There is a cluster of galaxies at $z = 0.245$ (MS 1308.8+3244; Stocke et al. 1991) in the error circle of the AMSSn source. The X-ray spectrum of the source is soft ($\Gamma_{\rm app} = +2.32 \pm 0.22$), and consistent with that of a cluster of galaxies. There are *ROSAT* HRI and PSPC sources detected in the error circle of the AMSSn source. There is no bright optical object in the *ROSAT* HRI error circle.

1AXG J132310–1656(SE34) — There is an NVSS source at the edge of the error circle of the AMSSn source. The optical counterpart of the NVSS source (21_04) is a broad-line AGN at $z = 0.022$. 45_01 is a narrow-emission line galaxy with HII-region like emission line ratios at $z = 0.135$ (see Figure 4). We identified this source with 21_04.

1AXG J133937+2730(NE17) — There is a *ROSAT* HRI source in the error circle of the AMSSn source. In the HRI error circle, there are three optical objects (44_00, 39_02, and 42_00). 42_00, at south-east in the HRI error circle, is a broad-line AGN at $z = 0.908$. 39_02 shows no emission line, and 44_00 is an M-type star. Thus, the AMSSn source is identified with the broad-line AGN.

1AXG J134412+0016(NE20) — There is a *ROSAT* PSPC source in the error circle of the AMSSn source. In the PSPC error circle, a FIRST radio source is detected. The optical counterpart of the radio source (17_00) is an emission line galaxy at $z = 0.452$. There is a hint of a broad-Hβ emission line, the X-ray source is identified with the AGN.

1AXG J134450+0005(NE19) — There is a *ROSAT* PSPC source in the error circle of the AMSSn source. The brightest object in the PSPC error circle (27_01) is identified with a broad-line AGN at $z = 0.087$.

1AXG J134741–1122(SE30) — The brightest object in the AMSSn error circle (19_01) is identified with a broad-line AGN at $z = 0.100$.

1AXG J140528+2224(NO15) — There is a *ROSAT* HRI source in the error circle of the AMSSn source. The optical counterpart of the HRI source (25_01) is a broad-line AGN at $z = 0.156$ (Mason et al. 2000; RXJ140528.3+222331).

1AXG J140532+5055(NO13) — There are 5 bright objects in and at the edge of the error circle of the AMSSn source. 24_00 is identified with a broad-line AGN at $z = 0.106$. 27_03 and AA show elliptical galaxy-like continua, and are at the same redshift as the broad-line AGN. 21_01 and 29_05 are Galactic stars. We identified this source with 24_00.

1AXG J141240−1209(SE03) — There is a *ROSAT* HRI source detected at the edge of the error circle of the AMSSn source. The optical counterpart of the HRI source (05_03) is identified with a broad-line AGN at $z = 0.247$.

1AXG J141343+4340(NE27) — There is a cluster of galaxies at $z = 0.089$ (Crawford et al. 1995; Abell 1885). The cD galaxy of the cluster, 35_05, is a narrow-line AGN (Crawford et al. 1995). The X-ray spectrum of the AMSSn source is soft ($\Gamma_{\rm app} = +2.39 \pm 0.07$) and consistent with that of clusters of galaxies. Thus the AMSSn source is identified with the cluster of galaxies.

1AXG J141426−1209(SE28) — There is a *ROSAT* HRI source in the error circle of the AMSSn source. The optical counterpart of the HRI source (14_02) is identified with a broad-line AGN at $z = 1.156$.

1AXG J142353+2247(NE09) — There is a *ROSAT* HRI source in the error circle of the AMSSn source. The optical counterpart of the HRI source (57_01) is identified with a narrow-line AGN at $z = 0.282$. For the line ratio diagnostic of the object, see Figure 4.

1AXG J142651+2619(NO51) — There is a *ROSAT* PSPC source in the error circle of the AMSSn source. The brightest object in the PSPC error circle (35_01) is identified with a broad-line AGN at $z = 0.258$. An NVSS source outside of the AMSSn error circle is identified with a narrow-line AGN at $z = 0.079$ (53_07). Because 35_01 is detected by PSPC and is closer to the center of the AMSSn source than 53_07, the AMSSn source is identified with 35_01.

1AXG J144055+5204(NE13) — There is a *ROSAT* PSPC source in the error circle of the AMSSn source. The brightest object in the PSPC error circle (42_02) is a broad-line AGN at $z = 0.320$ (Bade et al. 1995).

1AXG J144109+3520(NO32) — There is a *ROSAT* HRI source in the error circle of the AMSSn source. The optical counterpart of the HRI source (34_02) is identified with a narrow-emission line galaxy at $z = 0.077$. The line ratios of the narrow-emission lines are AGN-like (see Figure 4). 36_03 is an elliptical galaxy at the same redshift. The redshift difference of the two galaxies corresponds to the velocity difference of 1000 km s^{-1}.

1AXG J144301+5208(NO26) — There is a *ROSAT* HRI source at just outside of the error circle of the AMSSn source. The optical counterpart of the HRI source is identified

with an Me-type star. The HRI source is faint, and if typical X-ray spectrum of stars ($\Gamma_{\rm app}$ $> +2$) is assumed, the expected hard band flux is well below the AMSSn survey limit. There is another *ROSAT* HRI source 1.′6 south-west from the center of the AMSSn source. It is 3 times fainter than the former one. A FIRST radio source in the error circle of the AMSSn source is identified with a narrow-emission line galaxy. The large [OIII] to Hβ flux ratio is consistent with narrow-line AGN. Considering that the X-ray spectrum of the AMSSn source is hard ($\Gamma_{\rm app} = +1.01 \pm 0.18$) and the HRI sources are faint, The AMSSn source is identified with the narrow-line AGN.

1AXG J145026+1857(NO33) — There is a *ROSAT* PSPC source just outside of the error circle of the AMSSn source. There is a clustering of galaxies around the PSPC source, and the X-ray spectrum of the AMSSn source is soft ($\Gamma_{\rm app} = +2.17 \pm 0.17$). Thus the AMSSn source is identified with a cluster of galaxies. The redshift of the cluster is not available.

1AXG J150339+1016(NO05) — There is a *ROSAT* PSPC source in the error circle of the AMSSn source. In the PSPC error circle, a FIRST radio source is detected. The optical counterpart of the FIRST source is identified with a narrow-emission line galaxy at $z = 0.095$. The line ratios of the narrow-emission lines are consistent with those of AGNs (Figure 4). The radio source shows core and lobe structure.

1AXG J150423+1029(NO04) — There is a *ROSAT* HRI source in the error circle of the AMSSn source. The optical counterpart of the HRI source is a broad-line AGN at $z = 1.839$ (Wilkes et al. 1983; PKS1502+106).

1AXG J150430+4741(NO12) — There is a *ROSAT* HRI source in the error circle of the AMSSn source. The optical counterpart of the HRI source (13_01) is identified with a broad-line AGN at $z = 0.822$. It is also detected in the NVSS and FIRST radio surveys.

1AXG J151441+3650(NE10) — There is a *ROSAT* HRI source in the error circle of the AMSSn source. The optical counterpart of the HRI source (13_02) is a broad-line AGN at $z = 0.371$ (Schmidt 1974; 4C+37.43).

1AXG J151524+3639(NO21) — There are three bright optical objects in the error circle of the AMSSn source. 12_03 is a narrow-emission line galaxy at $z = 0.324$. The line ratios of the narrow-emission lines are AGN-like (see Figure 4). 13_01 is an elliptical galaxy at $z = 0.3$. 15_02 is an M-type star. 13_01 could be a companion galaxy of 12_03.

1AXG J155810+6401(NO22) — There is a *ROSAT* HRI source in the error circle of the AMSSn source. The optical counterpart of the HRI source (12_01) is identified with a broad-line AGN at $z = 0.352$.

1AXG J160118+0844(NO53) — There is a *ROSAT* HRI source in the error circle of

the AMSSn source. The optical counterpart of the HRI source (AA) is a narrow-emission line object at $z = 0.606$. Considering large [OIII] to Hβ flux ratio and hardness of the X-ray spectrum ($\Gamma_{\rm app} = +0.93 \pm 0.32$), the object is identified as a narrow-line AGN.

1AXG J163538+3809(NO47) — There is a *ROSAT* PSPC source in the error circle of the AMSSn source. The brightest object in the PSPC error circle (10_01) is identified with a narrow-emission line galaxy at $z = 0.099$. The line ratios of the narrow-emission lines are AGN-like (Figure 4).

1AXG J163720+8207(NE08) — There is a *ROSAT* PSPC source in the error circle of the AMSSn source. There are two optical objects in the PSPC error circle. 22_07 is a narrow-emission line galaxy with HII-region like emission line ratios. AA shows no emission line. A bright galaxy outside of the PSPC error circle (32_08) is a broad-line AGN at $z = 0.041$. 22_07 is a companion galaxy of 32_08 with a velocity difference of 200 km s^{-1}.

1AXG J164045+8233(NE07) — There is a cluster of galaxies (Vikhlinin et al. 1998; No.183) at $z = 0.26$. The X-ray spectrum of the AMSSn source is soft ($\Gamma_{\rm app} = +2.05 \pm 0.18$) and consistent with those of clusters of galaxies. Thus, the AMSSn source is identified with the cluster of galaxies.

1AXG J170305+4526(NO35) — There is a *ROSAT* HRI source in the error circle of the AMSSn source. The optical counterpart of the HRI source (34_02) is identified with a broad-line AGN at $z = 0.171$.

1AXG J170548+2412(NE11) — There is a *ROSAT* HRI source in the error circle of the AMSSn source. The optical counterpart of the HRI source is a merging galaxy (20_05 and 20_04). 20_05 is a broad-line AGN at $z = 0.114$ (Stocke et al. 1991). 20_04 is a narrow-emission line galaxy with AGN-like line ratios (see Figure 4). Considering the [O III]λ5007 flux of 20_05 is 3 times larger than that of 20_04 and the HRI source position is closer to 20_05 than 20_04, the AMSSn source is identified with the broad-line AGN, 20_05.

1AXG J170730+2353(NO24) — This source is observed with *Chandra*. The optical counterpart of the *Chandra* source is identified with a narrow-emission line galaxy at $z = 0.245$. The line ratios of the narrow-emission lines are AGN-like (Figure 4).

1AXG J171125+7111(NO02) — There are two *ROSAT* HRI sources around the error circle of the AMSSn source. The south-eastern HRI source is two times brighter than the north-western one, and is detected also by RASS. Thus the AMSSn source is identified with the south-eastern HRI source. The optical counterpart of the south-eastern source (41_00) is a broad-line AGN at $z = 1.011$ (Appenzeller et al. 1998) and that of the north-western one (21_08) is an M-type star.

1AXG J171811+6727(NE21) — There is a RASS source in the error circle of the AMSSn source. An optical object near the RASS center position (49_03) is identified with a broad-line AGN at $z = 0.549$.

1AXG J172815+5013(NO23) — There is a *ROSAT* HRI source in the error circle of the AMSSn source. The optical counterpart of the HRI source (17_01) is IZw187. It is a BL Lac object at $z = 0.054$.

1AXG J172938+5230(NO10) — There are a RASS and *ROSAT* PSPC sources in the error circle of the AMSSn source. A bright optical object near the center of the RASS source (23_01) is identified with a broad-line AGN at $z = 0.278$.

1AXG J174652+6836(NO42) — There is a *ROSAT* PSPC source in the error circle of the AMSSn source. The optical counterpart of the PSPC source is an AGN (Kriss & Canizares 1982; VIIZw 742, 1E1747.3+6836). This is a merging galaxy with two knots. The southern knot is a broad-line AGN at $z = 0.063$. The northern knot shows no emission line and optical continuum similar to that of an elliptical galaxy. The redshift difference of the two knots corresponds to a velocity difference of 630 km s^{-1}.

1AXG J174943+6823(NO43) — There is a *ROSAT* PSPC source in the error circle of the AMSSn source. The optical counterpart of the PSPC source (26_01) is a narrow-emission line AGN at $z = 0.051$ (Iwasawa et al. 1997). The emission line ratios of the narrow emission lines are AGN-like.

1AXG J210738−0512(NO17) — There is a *ROSAT* HRI source in the error circle of the AMSSn source. The optical counterpart of the HRI source (AA) is identified with a broad-line AGN at $z = 0.841$.

1AXG J230719−1513(SE35) — There is a *ROSAT* PSPC source just outside of the error circle of the AMSSn source. There is a cluster of galaxies at $z = 0.111$ (Abell et al. 1989; Abell 2533) in the PSPC error circle. The X-ray spectrum of the AMSSn source is consistent with those of clusters of galaxies ($\Gamma_{\rm app} = +2.02 \pm 0.10$).

1AXG J230738−1526(SE14) — There is a *ROSAT* PSPC source just outside of the error circle of the AMSSn source. The brightest optical object in the PSPC error circle (19_04) is identified with a broad-line AGN at $z = 0.199$.

1AXG J232639+2205(NO48) — A bright galaxy (19_01) in the AMSSn error circle is identified with a broad-line AGN at $z = 0.151$.

1AXG J233200+1945(NO18) — This source is observed with *Chandra* and *XMM-Newton*. The optical counterpart of the *Chandra* source (AA) is a narrow-emission line

galaxy at $z = 1.416$. High ionization lines of [NeIV]λ2424 and [NeV]λ3426 are detected. Thus the object is classified as an AGN. There is a hint of broad MgII emission line.

1AXG J233253+1513(NO14) — A bright galaxy in the AMSSn error circle (18_01) is identified with a broad-line AGN at $z = 0.215$. 21_02 shows no emission line.

1AXG J234725+0053(NE23) — This source is observed with *XMM-Newton*. Three sources are detected near the *ASCA* source position. The brightest source is more than three times brighter than the other sources in 2–10 keV band and consistent with the *ASCA* flux, thus we regard the brightest source as the counterpart of the *ASCA* source. The X-ray spectrum of the source shows strong Fe emission line at redshift of 0.213 ± 0.006 (Ueda et al. in preparation). Assuming the redshift and the intrinsic photon index of 1.7, the X-ray spectrum is fitted with $N_{\rm H} = 2.5 \pm 0.5 \times 10^{22}$ cm^{-2}. The estimated intrinsic luminosity is $L_{2-10{\rm keV}} = 1.7 \times 10^{44}$ erg s^{-1}. The object is heavily obscured luminous AGN. No optical spectroscopy has been conducted for the optical counterpart of the *XMM-Newton* source (26_00). Other AMSSn AGNs with similar redshifts and $N_{\rm H}$ are identified with AGNs without broad Hβ emission line (e.g. Figure 10), the object would have similar optical spectrum. In the later discussions, we treat the object as a heavily obscured no broad Hβ AGN.

1AXG J235541+2508(NE28) — There is a bright G5 star with a V magnitude of 8.7 in the error circle of the AMSSn source. The soft spectrum of the AMSSn source ($\Gamma_{\rm app}$ $= +3.28 \pm 0.08$) and small hard X-ray to optical flux ratio are consistent with those of G-type stars.

1AXG J235554+2836(NO20) — There is a *ROSAT* PSPC source in the error circle of the AMSSn source. The brightest object in the PSPC error circle is a broad-line AGN at $z = 0.729$ (Olsen 1970; 4C+28.59). There is a *ROSAT* PSPC source just outside of the AMSSn error circle. The PSPC source is a galactic star. The X-ray spectrum of the AMSSn source ($\Gamma_{\rm app} = +1.61 \pm 0.18$) is too hard to be a galactic star, thus the AMSSn source is identified with the broad-line AGN.

3.4. Summary of Emission Line Diagnostics of the Observed Objects

In order to evaluate the strength and the width of detected emission lines, a spectral fitting for emission lines with the χ^2 minimization method is conducted. For the fitting, **specfit** command in **spfitpkg** package in the IRAF is applied. All the emission lines are fitted with Gaussian profile. For Hα and Hβ lines, we put one broad and one narrow components independently. We assume that the narrow Hα (narrow Hβ) line has the same velocity width as [N II]λ6583([O III]λ5007). FWHMs of line widths are deconvolved by the

spectral resolution mentioned in Section 3.2. The results are summarized in Table 4. In the table, equivalent widths of [O III]λ5007, broad Hβ, narrow Hβ, [N II]λ6583, broad Hα, and narrow Hα, and velocity widths of narrow [O III]λ5007, broad Hβ, and broad Hα are summarized. If the best-fit line flux is 3 times more than the estimated uncertainty of the line flux of a component, the best-fit line flux and the uncertainty is listed, otherwise one sigma upper limit for a component is listed. The upper limits for broad lines and narrow lines are determined by assuming velocity width of 3000 km s^{-1} and 500 km s^{-1}, respectively.

Two thirds of the AMSSn sources (60/87) have optical counterparts with a significant ($> 3\sigma$, except for 1AXG J134412+0016(NE20), see Section 3.3) broad emission line either in Hα, Hβ, Mg IIλ2800, C III]λ1909, C IVλ1549, or Lyα. The velocity width of the broad Hβ emission line versus the $\Gamma_{\rm app}$ is plotted in Figure 3. There is no population of narrow-line Seyfert 1s which show small Hβ line width (< 2000 km s^{-1}) and large $\Gamma_{\rm app}$ (> 2) (Brandt, Mathur & Elvis 1997).

Optical counterparts of 15 AMSSn sources only show narrow-emission lines whose line ratios are consistent with those of Seyfert galaxies. For 9 of them, both Hα and Hβ wavelength ranges are observed. The distribution of the [N II]λ6583 to Hα and [O III]λ5007 to Hβ ratios of the 9 objects is shown in Figure 4 (solid squares).[4] The regions enclosed by the solid lines represent the regions occupied by Seyfert galaxies, LINERs, and HII-region like galaxies in the diagram (Veilleux & Osterbrock 1987). All 9 objects fall in the region of Seyfert galaxies. As for the 6 remaining objects, 1AXG J174943+6823(NO43) is identified with a narrow-line AGN (Seyfert) by Iwasawa et al. (1997), and detailed discussion on the narrow-line ratios of the object, see the paper. 1AXG J233200+1945(NO18) shows high ionization narrow lines of [NeIV]λ2424 and [NeV]λ3426, thus we identify the object with a narrow-line AGN. It also shows a hint of a broad MgIIλ2800 emission line. For the remaining 4 narrow-line galaxies, only [O III]$\lambda\lambda$5007,4959 narrow-emission lines are detected. The logarithmic lower limits on [O III]λ5007 to Hβ flux ratio are 1.0 for 1AXG J123605+2613(NE04), 1.1 for 1AXG J144301+5208(NO26), 1.4 for 1AXG J151524+3639(NO21), and 1.5 for 1AXG J160118+0844(NO53). The lower limits are consistent with Seyfert-like line ratios. All of the identified narrow-line galaxies are Seyfert-like galaxies, and there is no candidate of an optical counterpart with LINER-like emission line ratios.

Narrow-emission line ratios of broad-line AGNs with strong narrow-emission lines are

[4] In the diagram, we plot narrow-emission line galaxies which are spectroscopically observed, but not identified with an X-ray source (cross). They are mostly serendipitous galaxies with HII-region like narrow-emission line ratios. Two objects, 53_07 of 1AXG J142651+2619(NO51) and 20_04 of 1AXG J170548+2412(NE11) have line ratios consistent with Seyfert galaxies. Since the two X-ray sources are identified with broad line AGNs, we regard 53_07 and 20_04 to be serendipitous narrow line AGNs.

also plotted with open squares. Most of the broad-line AGNs also have narrow-line ratios similar to Seyfert galaxies, as we expect. 1AXG J111518+4042(NO56) and 1AXG J140532+5055(NO13) have small [O III]λ5007 to Hβ flux ratios and their line ratios fall amongst those of LINERs. Since they have the narrower broad Hβ lines than other broad-line AGNs in the diagram, contamination by broad Hβ line possibly causes the small [O III]λ5007 to Hβ line ratios.

3.5. Reliability of the Identifications

All but one of the 87 AMSSn hard X-ray selected sources are optically identified with either AGNs (including broad-line AGNs, narrow-line AGNs, and BL Lac objects (3)), clusters of galaxies (7), or a galactic star (1). Distribution of the distances between the optical counterparts and the X-ray sources normalized by 90% error radius is shown in Figure 5. 90% of the optical counterparts are located within the estimated 90% error radius, thus the distribution of the optical counterparts is consistent with the estimated uncertainties of the AMSSn X-ray source positions.

Based on optically-selected broad-line AGN counts (Hartwick & Schade 1990), the number of broad-line AGNs which fall in the error circles by chance can be estimated. The total uncertainty area that is sum of the areas of the error circles of the AMSSn sources except for the sources whose error circles are tightly constrained by either *Chandra* or *ROSAT* HRI is 167 arcmin^2. Most of the identified broad-line AGNs are brighter than R of 19 mag corresponding to B of 19.5 mag for a typical QSO color ($B - R = 0.5$ mag). The cumulative number density of broad-line AGNs brighter than B of 19.5 mag with redshift smaller than 2.2 is 8.5 degree^{-2} (Hartwick & Schade 1990). Thus, the expected number of contamination by broad-line AGNs is 0.4. It should be noted that positional information from *ROSAT* PSPC and NVSS and FIRST radio sources is used for a part of the sources, thus the number should be smaller. Therefore we conclude that the contamination by chance coincidence is negligible.

For 15 AGNs showing only narrow-emission lines, 11 of them are observed by either *Chandra*, *ROSAT* HRI, NVSS, or FIRST, and the identifications are reliable. The remaining 4 objects are brighter than 18.5 mag in R band, and they show strong [O III]$\lambda\lambda$5007,4959 emission lines. The number density of field galaxies at the magnitude is about 100 degree^{-2} (see e.g, Yasuda et al. 2001). About 40% of the field galaxy population show strong [O III]$\lambda\lambda$5007,4959 emission lines at B of 19 mag (Madgwick et al. 2002) (it corresponds roughly R of 18 mag), and 17% of field emission line galaxies show AGN-like emission lines (Tresse et al. 1996). Therefore, the number density of AGN-like narrow-emission line galax-

ies brighter than R of 18.5 mag is estimated to be 7 degree^{-2}, and the expected number of contamination of such galaxies in 167 arcmin^2 field is 0.32, and it is negligible.

There are 7 candidates of a cluster of galaxies in the AMSSn sample. Redshifts of the 6 candidates are known, and they range from 0.073 to 0.260. X-ray spectra of all of the 7 clusters of galaxies are consistent with a soft X-ray spectrum of clusters of galaxies. With the number of clusters of galaxies (7 ± 2.6) and the survey area (Section 2), the number density of clusters of galaxies above 3×10^{-13} ergs s^{-1} cm^{-2} in the 2–10 keV band is estimated to be $\log N(> S) = -0.9 \pm 0.2$ degree^{-2}. It is consistent with that determined in the ALSS with 2 clusters of galaxies at the same flux limit ($\log N(> S) = -0.9^{+0.2}_{-0.5}$ degree^{-2}; AOY00). This consistency supports the idea that the identifications of clusters of galaxies are also reliable.

3.6. Comparison with Other Hard X-ray Selected AGN Samples

The hard X-ray to optical flux ratio is one of basic properties which reflect the nature of the detected objects. In Figure 6, the optical magnitudes and the 2–10 keV hard X-ray fluxes of the AMSSn AGNs (open circle) are compared with those of hard X-ray selected AGN samples from *HEAO1* A2 survey (open triangle; Piccinotti et al. 1982), ALSS (open square; AOY00), *Beppo-SAX* HELLAS survey (small dots; La Franca et al. 2002) and *Chandra* survey of CDFN (Brandt et al. 2001; Barger et al. 2002) and of CDFS (Giacconi et al. 2002) (asterisks and filled triangles for upper limits). The HELLAS survey is done in the 5–10 keV band, and the flux in the energy band is converted to the 2–10 keV flux, with the photon index of typical AGNs ($\Gamma = 1.7$; e.g. Inoue 1985). The 2–8 keV band is used as the hard band in the CDFN survey, the 2–8 keV flux is converted to the 2–10 keV flux with the effective photon index of each source. The *Chandra* objects do not necessarily show AGN-like emission lines in the optical wavelength, but their hard X-ray emissions are thought to originate from AGNs. The X-ray to optical flux ratio is determined by $\log f_{2-10\ \mathrm{keV}}/f_{\mathrm{R}} = \log f_{2-10\ \mathrm{keV}} + R/2.5 + 5.5$ which is derived with Kron-Cousin R band response function (Hornschemeier et al. 2001). The distribution of hard X-ray to optical flux ratios of AMSSn AGNs is similar to those of other hard X-ray selected samples. AMSSn, ALSS and HELLAS samples have similar flux limits and their ranges of X-ray to optical flux ratio are consistent with each other ($\log f_{2-10\ \mathrm{keV}}/f_R = -2 - +2$). The range is larger than that of *HEAO1* A2 sample ($\log f_{2-10\ \mathrm{keV}}/f_R = -0.5 - +1$). The deep *Chandra* samples have a larger range than the *ASCA* samples ($\log f_{2-10\ \mathrm{keV}}/f_R = -4 - +3$). A significant number of AMSSn AGNs have hard X-ray to optical flux ratios as large as the optically-faint hard X-ray source seen in deep *Chandra* surveys ($\log f_{2-10\ \mathrm{keV}}/f_R > +1$). The optically-faint objects are candidates of high-redshift absorbed AGNs (Section 4.2.2).

As mentioned in Section 1, the distribution of the AMSSn AGNs in the redshift versus hard X-ray luminosity diagram is different from deep *Chandra* sample of AGNs. In order to compare the distributions of hard X-ray selected AGNs, the redshift and hard X-ray luminosity of the AMSSn, ALSS (AOY00), *HEAO1* A2 (Piccinotti et al. 1982), and *Chandra* CDFN (Brandt et al. 2001; Barger et al. 2002) samples of AGNs are plotted in Figure 7. From the CDFN sample, only spectroscopically identified objects are plotted. The 2–10 keV intrinsic luminosity, $L_{2-10\mathrm{keV}}$, of each AMSSn AGN is calculated by correcting for the redshift (k-correction), the Galactic absorption, and the estimated intrinsic absorption to the nucleus. The intrinsic absorption is estimated from the hardness ratio corrected for Galactic absorption and the instrument response, assuming that intrinsic nuclear emission of AGNs is a power-law spectrum with photon index of 1.7 (Section 4.1). For AGN with apparent X-ray spectra softer than Γ_{app} of 1.7, the luminosity is calculated with the best fit power-law index. The estimated luminosities are listed in Table 3. The 2–10 keV luminosities of the CDFN objects are calculated in the same way as those for AMSSn AGNs using Γ_{app} in the 0.5–8 keV, count rate in the hard band, and response function of *Chandra* ACIS. The intrinsic photon index is assumed to be 1.7 (Section 4.1). The redshift range of the AMSSn and ALSS samples of AGNs is similar to that of CDFN sample, but their luminosity is typically 2 orders of magnitude larger than CDFN sample at the same redshift. The AMSSn sample consists of Seyfert galaxies ($L_{2-10\mathrm{keV}} < 1 \times 10^{44}$ ergs s^{-1}) at redshifts around 0.1 and QSOs ($L_{2-10\mathrm{keV}} > 1 \times 10^{44}$ ergs s^{-1}) at higher redshifts up to 2. Thus *ASCA* selected samples of AMSSn and ALSS AGNs are suitable to study luminous AGNs (QSOs) in the intermediate redshift universe.

4. ABSORPTION TO THE NUCLEUS IN THE HARD X-RAY SELECTED AGNS

4.1. Absorption to the Nucleus Estimated by X-ray Hardness

A significant fraction of the identified AGNs in the AMSSn and ALSS show hard X-ray spectra. The redshift versus Γ_{app} diagram of the identified AGNs is shown in Figure 8 along with ALSS AGNs. More than 80% of the AMSSn and ALSS AGNs lie Γ_{app} between 1 and 2.5, but 11 objects have Γ_{app} smaller than 1 in the AMSSn and ALSS AGNs. Absorption to their nuclei is thought to make their X-ray spectra very hard. With the X-ray spectrum of each source, the amount of the X-ray photoelectric absorption to the source can be estimated by assuming the intrinsic spectrum and adopting the redshift of the source.

Distributions of 0.7–10 keV apparent photon index, Γ_{app} of the AMSSn and ALSS AGNs are shown in Figure 9. The Γ_{app} distributions of AMSSn and ALSS samples above Γ_{app} of 1

are consistent with a Gaussian distribution with an average photon index of 1.7 and a sigma of 0.2 comparable to the uncertainties of the $\Gamma_{\rm app}$ determinations for objects with $\Gamma_{\rm app} > 1$ (Table 2). The average photon index is consistent with that determined in the CDFN survey ($\Gamma = 1.7$ in the 0.5–8 keV band; Barger et al. 2002), and in the *XMM-Newton* observation of Lockman Hole AGNs ($\Gamma = 1.9 \pm 0.9$ in the 0.5–10 keV band; Mainieri et al. 2002). Therefore a power-law with photon index of 1.7 is used as the intrinsic X-ray spectrum of AGNs.

The conversion from the $\Gamma_{\rm app}$ to the amount of the absorption depends on the redshift, because higher-energy photons of the source frame is observed at higher redshift. In Figure 8, the upper and lower solid lines in the figure correspond to the $\Gamma_{\rm app}$ of an object at the redshift with the intrinsic photon index of 1.7 and X-ray absorption with hydrogen column densities, $N_{\rm H}$, of 1×10^{22} cm^{-2} and 1×10^{23} cm^{-2}, respectively. The X-ray sources with $\Gamma_{\rm app}$ smaller than 1 correspond to AGNs at intermediate redshifts affected by X-ray absorption with $N_{\rm H}$ of 1×10^{22} cm^{-2} $-$ 1×10^{23} cm^{-2}, and high-redshift AGNs with $N_{\rm H} > 1 \times 10^{23}$ cm^{-2}.

The estimated absorption is listed in Table 3, and plotted as a function of absorption-corrected luminosity in Figure 10 for $z < 0.6$(a) and $z > 0.6$(b) AGNs, along with ALSS AGNs respectively. At $z < 0.6$, five luminous ($L_{2-10{\rm keV}} > 1 \times 10^{44}$ erg s^{-1}) absorbed ($N_{\rm H} > 1 \times 10^{22}$ cm^{-2}) AGNs are found in the AMSSn sample. At $z > 0.6$, there are two AGNs with $L_{2-10{\rm keV}} > 1 \times 10^{45}$ erg s^{-1} and $N_{\rm H} > 1 \times 10^{23}$ cm^{-2}. These objects are candidates of long-sought absorbed luminous AGNs (type-2 QSOs).

4.2. Relation between X-ray and Optical Properties

The large column density of absorbing material ($> 1 \times 10^{22}$ cm^{-2}) inferred from the hard X-ray spectrum can contain large amount of dust, and should affect the optical properties of the AGNs, i.e. apparent strength of broad lines, faintness of the optical continuum, and redness of the optical and near-infrared continuum. The strength of broad lines, the X-ray-to-optical flux ratio, and the near-infrared colors are discussed in the following subsections.

4.2.1. Strength of Broad Lines

If broad emission lines are present in all AGNs, the non-detection of these lines should imply the presence of significant amount of dust along our line-of-sight (Antonucci 1993). For more than half of the AMSSn and ALSS AGNs, that is all of the AMSSn and ALSS AGNs at $z < 0.6$, Hβ emission lines are measured by our observation, thus we use the emission line as an indicator. In Figure 8 and 10(a), AMSSn and ALSS AGNs without significant broad Hβ

line (no broad Hβ AGNs) are marked with large crosses. Most of the AGNs with hard X-ray spectra do not show broad Hβ emission, and the no broad Hβ AGNs have significantly larger $N_{\rm H}$ than that of the broad Hβ AGNs. The Kolmogorov-Smirnov test (K-S test) indicates that the $N_{\rm H}$ distribution of the no broad Hβ AGNs is different from that of the broad Hβ AGNs with 99.9% confidence.

Among AGNs at $z > 0.6$, 1AXG J160118+0844(NO53) and 1AXG J233200+1945(NO18) do not show strong broad emission lines, and strong narrow emission lines are detected. $N_{\rm H}$ estimated from X-ray spectra are $(3 \pm 2) \times 10^{22}$ cm^{-2} and $(10 \pm 5) \times 10^{22}$ cm^{-2}. Therefore, they are candidates to be the luminous cousins of type-2 Seyferts at high-redshifts, i.e. type-2 QSOs. The other high-redshift AGNs show strong broad emission lines of either Mg IIλ2800, C III]λ1909 or Lyα. 1AXG J133937+2730(NE17), 1AXG J150423+1029(NO04), and 1AXG J210738$-$0512(NO17) show strong broad emission lines, although they are estimated to have $N_{\rm H} > 1 \times 10^{22}$ cm^{-2}. The $N_{\rm H}$ corresponds to an extinction of more than 10 magnitude at the wavelength of Mg IIλ2800 with the Galactic $N_{\rm H}$ to A_V ratio ($N_{\rm H}/A_V = 1.79 \times 10^{21}$cm^{-2}; Predehl & Schmitt 1995) and the Galactic extinction curve ($A_{2800\mathring{A}}/A_V = 1.9$; Cardelli, Clayton, & Mathis 1989). The broad emission lines would not be detected through such a large absorbing column, implying a different line of sight to the X-ray source, dust-free material (e.g. dust sublimation in warm absorbing gas) or different dust properties (e.g. different dust size distribution in AGNs; Maiolino et al. 2001a,b). Similar AGNs with broad emission lines and large $N_{\rm H}$ are summarized in Maiolino et al. (2001a). There is another possibility that their optical nuclei are obscured and the broad lines come from scattered nuclear light (Aligheri et al. 1994; Akiyama & Ohta 2001). It is also possible that their intrinsic X-ray spectra are harder than a power-law with a photon index of 1.7 and the estimated large amount of X-ray absorption is not real. A reflection component is often present in Seyfert galaxies above 6 keV and may explain the hardening of the X-ray spectrum of high-redshift QSOs (AOY00).

4.2.2. Hard X-ray to Optical Flux Ratio

AGNs which have large hard X-ray to optical flux ratio ($\log f_{2-10\ {\rm keV}}/f_R > +1$) are marked with small dots in Figure 8 and 10. Six out of 10 of the optically-faint AMSSn and ALSS AGNs are at $z > 0.6$. In the redshift range, the objects with $\Gamma_{\rm app} < 1$ are optically faint and X-ray bright and are consistent with absorption in the optical/UV. Three of the broad-line AGNs with $N_{\rm H} > 1 \times 10^{22}$ cm^{-2} mentioned in the previous subsection also have large hard X-ray to optical flux ratio suggesting dust absorption in the optical continuum

emission. It should be noted that 5/10 of the optically-faint AGNs are radio-loud AGNs. It is consistent with the fact that radio-loud AGNs have larger X-ray to optical flux ratio on average (Zamorani et al. 1981).

4.2.3. Near-infrared Color

The near-infrared color of an AGN can be another indicator of the amount of dust absorption to the nucleus. About two thirds of the AMSSn AGNs (48/76) and all of the ALSS AGNs are covered in the area of the second incremental database of the Two Micron All Sky Survey (2MASS; Kleinmann et al. 1994). The 2MASS is an all sky survey in the J-, H-, and K_S- bands down to J of 16.5 mag, H of 15.5 mag, and K_S of 15.0 mag. In the covered AGNs, $56 \pm 6\%$ (44/78) of them are detected in the survey. The J-, H-, and K_S-bands magnitudes of detected AMSSn AGNs are listed in Table 2. The $J - K_S$ colors of the AMSSn and ALSS AGNs are plotted as a function of redshift in Figure 11. The $J-K_S$ colors of optically-selected AGNs (Barkhouse & Hall 2001) and *HEAO1* A2 AGNs (Kotilainen et al. 1992) are also plotted in the same figure with small dots and small crosses, respectively. At redshifts smaller than 0.3, elliptical galaxies (solid line, no evolution is considered) are bluer than AGNs, thus the contribution from the host galaxy of an AGN make its color bluer than a typical AGN. At redshift smaller than 0.2, the color distribution of the AMSSn and ALSS AGNs is bluer and closer to the track of an elliptical galaxy than that of *HEAO1* A2 AGNs on average. Above this redshift, the color range of the AMSSn AGNs is similar to that of optically-selected AGNs.

The criteria of $J - K_S$ color redder than 2 is used for selecting red QSOs in the 2MASS survey. There are four AGNs with $J - K_S$ color redder than 2 in the AMSSn AGNs. No AGNs in the ALSS sample have $J - K_S$ color redder than 2. The $J - K_S$ colors (≤ 3) and redshift range ($z \leq 0.7$) of the red AGNs are similar to those of the 2MASS red QSO population (Wilkes et al. 2002). The $J - K_S$ color of 1AXG J121854+2957(NO07) is very red: 1.0 magnitude redder than the average of optically-selected AGNs, and 1.8 magnitude redder than the bluest AMSSn AGN at the redshift of 0.2. If it is assumed that the dust absorption to the nucleus causes the red $J-K_S$ color of the object, and intrinsic $J-K_S$ color is similar to those of 2MASS and AMSSn AGNs at the same redshift ($1.2 < J - K_S < 2.4$), the amount of dust absorption to the nucleus is estimated to be A_V of $3 - 9$ mag at the object frame with the Galactic extinction curve. With the Galactic A_V to $N_{\rm H}$ ratio, the estimated amount of dust absorption can be converted to X-ray absorption column density of $(1 - 2) \times 10^{22}$ cm^{-2}, which is roughly consistent with that calculated from the X-ray hardness [$(3 \pm 1) \times 10^{22}$ cm^{-2}]. The amount of the X-ray absorption to the nucleus is also

similar to those observed in 2MASS red AGNs (Wilkes et al. 2002).

At $z > 0.3$, large fraction of AMSSn and ALSS AGNs are not detected in the 2MASS survey (plotted at $J - K_S < 0$ in Figure 11), because the 2MASS survey limit is not deep enough to detect them. We conducted near-infrared photometric observations of AMSSn and ALSS AGNs not detected in the 2MASS survey to assess the fraction of red QSOs. The results will appear elsewhere.

4.3. Luminosity Distributions of Absorbed and Unabsorbed AGNs

The luminosity distribution of less-absorbed ($N_{\rm H} < 1 \times 10^{22}$ cm^{-2}) and absorbed ($N_{\rm H} > 1 \times 10^{22}$ cm^{-2}) AGNs are compared in Figure 12. We combined samples of AMSSn, ALSS and *ASCA* Deep Survey in the Lockman Hole (ADSL; Ishisaki et al. 2001). ADSL sample consists of 12 hard X-ray selected AGNs above flux limit of 3×10^{-14} ergs s^{-1} cm^{-2}(Ishisaki et al. 2001). Because at high redshifts, AGNs with $N_{\rm H} = 1 \times 10^{22}$ cm^{-2} can not be distinguished from AGNs without absorption (Figure 8), we limit the sample of AGNs up to redshift of 0.6. Below this redshift, Hβ wavelength is covered for all AGNs. The fraction of the absorbed AGNs in the luminous AGNs with $L_{2-10{\rm keV}} > 3 \times 10^{45}$ ergs s^{-1} (1/13, 8 ± 8%) is smaller than that in the less-luminous AGNs with $L_{2-10{\rm keV}} < 3 \times 10^{45}$ ergs s^{-1} (14/70, 20 ± 5%). But, the K-S test on the luminosity distributions of absorbed and less-absorbed AGNs indicates that there is no significant difference between the two luminosity distributions (86% significance).

In order to extend the comparison to lower intrinsic luminosity range, we combined the hard X-ray selected *Chandra* CDFN AGNs (Barger et al. 2002). Spectroscopic redshifts are available only for objects brighter than R of 24 mag, thus optical spectroscopic identification of CDFN is not complete, especially for high-redshift absorbed AGNs. The spectroscopic identification is also limited by the fact that strong emission lines go out of optical wavelength at redshifts larger than 1.4. For objects without spectroscopic redshifts, their photometric redshifts are used, and we also limit the sample up to redshift of 0.6. Intrinsic absorption and luminosity of the AGN is estimated with the $\Gamma_{\rm app}$ in the 0.5–8 keV by assuming an intrinsic photon index of 1.7 in the same way as those for AMSSn AGN. The luminosity distributions of less-absorbed and absorbed AGNs are compared combining the *ASCA* and CDFN samples. The less-absorbed AGNs marginally have larger luminosity than absorbed AGNs; the K-S test shows that the luminosity distributions of less-absorbed and absorbed AGNs are marginally different with 98% confidence. The marginal differences of luminosity distribution of absorbed and less-absorbed AGNs may indicate that the fraction of absorbed AGNs decreases with increasing intrinsic luminosity.

In order to evaluate the *intrinsic* fraction of absorbed AGNs, the detection limit of 2–10 keV selection has to be corrected. In the AMSSn AGNs, since the sample is limited by the count rate, the limit to the intrinsic luminosity at each redshift depends on the amount of absorption. Detailed evaluation of the luminosity function of less-absorbed and absorbed AGNs and the estimation of the *intrinsic* fraction of absorbed AGNs are discussed in a separate paper (Ueda et al. 2003).

As summarized in Section 4.2.1, the non-detection of the broad Hβ emission line can be used as an indicator of dust absorption to the nucleus. The luminosity distribution of broad Hβ and no broad Hβ AGNs in the AMSSn, ALSS, and ADSL are compared in Figure 13. The luminosity distribution of the broad Hβ AGNs is also marginally different from that of the no broad Hβ AGNs. K-S test indicates that the broad Hβ AGNs have larger intrinsic luminosity than the no broad Hβ AGNs with 97% confidence. It is suggested that the fraction of no broad Hβ AGNs in QSOs is smaller than that in the Seyfert galaxies. Such luminosity dependence of the fraction of narrow-line AGNs is also reported in a radio selected sample of AGN (e.g. Lawrence 1991) and a far-infrared selected sample (e.g. Barcons et al. 1995).

5. RADIO PROPERTIES OF THE AMSSN AGNS

Radio loudness is one of important properties of AGNs. $37 \pm 5\%$(29/79) AMSSn AGNs including 3 BL Lac objects are detected either in the NVSS or FIRST survey. The detection rate is similar to that in the ALSS ($33 \pm 9\%$; 10/30). The optical and radio luminosities, and hard X-ray and radio luminosities of the AMSSn AGNs (circles) are plotted in Figures 14 and 15. The 1.4GHz radio luminosity of each source is calculated from the 1.4 GHz NVSS flux of the source assuming a power-law radio spectrum with index of -0.5. If the FIRST flux is available, the flux is used for the calculation. For AGNs without NVSS detection, the upper limits on the radio luminosities are calculated with the detection limit of NVSS (2.5mJy), and indicated with downward arrows. ALSS AGNs (squares) are also plotted in the figures. In Hooper et al. (1996), AGNs above the dashed line in Figure 14 are defined as radio-loud AGNs ($R_{8.4} \equiv \log L_{8.4}/L_B > +1$). $L_{8.4}$ and L_B of AMSSn and ALSS AGNs are derived from $L_{1.4}$ and M_V by assuming power-law index of -0.5. Following the radio-loudness criterion, the number of radio-loud AGNs is 20 excluding AGNs with radio upper limit, and the fraction is $18 \pm 4\%$ (20/109) in the AMSSn and ALSS AGNs.

The optical luminosity is affected by dust absorption, and the radio to optical luminosity ratio may not be a good indicator of intrinsic radio-loudness. In Figure 15, the AMSSn AGNs satisfying the above radio-loud criterion are marked with large squares. Typical hard-X-ray to radio luminosity ratio in QSOs are shown with dashed lines for radio-loud QSOs (upper)

and radio-quiet QSOs (lower) (Elvis et al. 1994). In the distribution of the AMSSn and ALSS AGNs, there is a clear gap of 1 order of magnitude below the radio-loud QSO line. There are four AGNs located within the scatter of radio-quiet AGNs, but are identified as radio-loud AGNs from their radio to optical flux ratios. If the sample is divided at the solid line, there are 17 radio-loud AGNs in the AMSSn and ALSS AGNs, thus the fraction of radio-loud AGNs is $16 \pm 4\%$ in total. The fraction is higher than that in the *ASCA* LSS sample of AGNs (10%, AOY00).

The fraction of the radio-loud objects increases as the X-ray luminosity increases; $10{\pm}5\%$ (4/41) and $43 \pm 11\%$ (9/21) for AGNs with $3 \times 10^{41} < L_{2-10\mathrm{keV}} < 1 \times 10^{44}$ ergs s^{-1}and $1 \times 10^{45} < L_{2-10\mathrm{keV}} < 3 \times 10^{46}$ ergs s^{-1}, if we define radio-loudness with radio to X-ray luminosity ratio. A K-S test comparing the $L_{2-10\mathrm{keV}}$ distribution of radio-loud objects and that of radio-quiet objects shows that the two distribution is different with >99.95% confidence. A similar tendency is also detected in the Palomar-Green Bright Quasar Survey and the Einstein Extended Medium Sensitivity Survey (Hooper et al. 1996). In the EMSS sample of AGNs, all but one radio-loud AGNs have 0.3–3.5 keV luminosities, $L_{0.3-3.5\mathrm{keV}} > 1{\times}10^{44}$ erg s^{-1}, even though many radio-quiet QSOs have $L_{0.3-3.5\mathrm{keV}} < 1{\times}10^{44}$ erg s^{-1} (Della Ceca et al. 1994). The tendencies are consistent with the fact that radio-loud QSOs have 3 times larger hard X-ray luminosity than radio-quiet QSOs at a given optical luminosity (Zamorani et al. 1981).

6. SUMMARY

We have presented the results of optical spectroscopic identifications of a bright sub-sample of hard X-ray selected sources from the AMSS in the northern sky (AMSSn). The total survey areas are 34 degree^2 and 68 degree^2 at flux limits of 3×10^{-13} ergs s^{-1} cm^{-2} and 1×10^{-12} ergs s^{-1} cm^{-2} in the 2–10 keV band, respectively. All of the 87 hard X-ray selected sources are identified, with AGNs (including broad-line AGNs, narrow-line AGNs, and 3 BL Lac objects), 7 clusters of galaxies, and 1 galactic star. It is the largest complete sample of hard X-ray selected AGNs at the bright flux limit. The AMSSn AGNs consists of Seyfert galaxies at redshifts around 0.1 and QSOs at higher redshifts up to 2. Their luminosities are typically two orders of magnitude larger than the deep CDFN sample, and the AMSSn AGNs sample is suitable to study luminous AGNs in the intermediate redshift universe.

Amounts of absorption to the nuclei of the AGNs are estimated at hydrogen column densities of up to $\sim 3 \times 10^{23}$ cm^{-2} from their X-ray spectra. There are several candidates of luminous ($L_{2-10\mathrm{keV}} > 1 \times 10^{44}$ ergs s^{-1}) absorbed ($N_{\mathrm{H}} > 1 \times 10^{22}$ cm^{-2}) AGNs, i.e., type-2 QSOs. Optical properties of X-ray absorbed AGNs with $N_{\mathrm{H}} > 1 \times 10^{22}$ cm^{-2} indicate the

effects of dust absorption. At $z < 0.6$, most of the X-ray absorbed AGNs do not show broad Hβ emission lines. At $z > 0.6$, the X-ray absorbed AGNs show large hard X-ray to optical flux ratios ($\log f_{2-10\ \mathrm{keV}}/f_R > +1$). However, three high-redshift AGNs with strong broad lines show hard X-ray spectra with $N_{\mathrm{H}} > 1 \times 10^{22}$ cm^{-2}. The column density corresponds to extinction of more than 10 mag at the wavelength of Mg IIλ2800 with Galactic N_{H} to A_V ratio and Galactic extinction curve, and the strong broad lines would not be detected.

In combination with hard X-ray selected AGN samples from the *ASCA* Large Sky Survey, the *ASCA* Deep Survey in the Lockman Hole and CDFN, the luminosity distribution of absorbed ($N_{\mathrm{H}} > 1 \times 10^{22}$ cm^{-2}) and less absorbed ($N_{\mathrm{H}} < 1 \times 10^{22}$ cm^{-2}) AGNs are compared at $z < 0.6$. There is a marginal difference of luminosity distributions of absorbed and less-absorbed AGNs, it may indicate that the fraction of absorbed AGNs decreases with increasing intrinsic luminosity.

7. NOTE ADDED IN PROOF

We conducted an optical spectroscopic observation of the optical counterpart of 1AXG J234725+0053(N with FOCAS on Subaru telescope. The object shows AGN-like emission lines at $z = 0.233 \pm 0.001$, which is slightly larger than that determined from the X-ray spectrum. No broad Hβ emission line is detected.

A follow-up observation of 1AXG J133937+2730(NE17) with XMM-Newton detected two X-ray sources in the error circle. The coordinates are $13^{\mathrm{h}}\ 39^{\mathrm{m}}\ 36^{\mathrm{s}}\ +27^{\circ}\ 30'\ 48''$ and $13^{\mathrm{h}}\ 39^{\mathrm{m}}\ 39^{\mathrm{s}}\ +27^{\circ}\ 30'\ 24''$. In the text, we identified the ASCA source with the latter one. However, the former one is 2.5 times brighter than the latter one in the 2–10 keV band. The former one is associated with a galaxy.

We would like to thank members of UH88″ telescope, KPNO, and Subaru Telescope team, especially, Dr. Youichi Ohyama, who gave us opportunity to observe an object and advice on FOCAS observing run. We appreciate the help of Drs. Akihiko Tomita and Ingo Lehmann for the spectroscopic identification. We are grateful to anonymous referee for invaluable comments. We thank Dr. Chris Simpson for helpful comments that improved the manuscript. This publication makes use of data products from the Two Micron All Sky Survey, which is a joint project of the University of Massachusetts and the Infrared Processing and Analysis Center/California Institute of Technology, funded by the National Aeronautics and Space Administration and the National Science Foundation. This research has made use of the NASA/IPAC Extragalactic Database (NED) which is operated by the Jet Propulsion Laboratory, California Institute of Technology, under contract with the National Aeronautics

and Space Administration, and data obtained from the High Energy Astrophysics Science Archive Research Center (HEASARC), provided by NASA's Goddard Space Flight Center.

REFERENCES

Abell, G.O., Corwin, H.G., & Olowin, R.P. 1989, ApJS, 70, 1

Akiyama, M., et al. 2000, ApJ, 532, 700 [AOY00]

Akiyama, M., & Ohta, K. 2001, PASJ, 53, 63

Alexander, D.M., Brandt, W.N., Hornschemeier, A.E., Garmire, G.P., Schneider, D.P., Bauer, F.E, & Griffiths, R.E. 2001, AJ, 122, 2156

Allington-Smith, J. R., Lilly, S. J., & Longair, M. S. 1985, MNRAS, 213, 243

Alighieri, S. S., Cimatti, A., & Fosbury, R.A.E. 1994, ApJ, 431, 123

Antonucci, R. 1993, ARA&A, 31, 473

Appenzeller, I., et al. 1998, ApJS, 117, 319

Arakelian, M. A., Dibay, E. A., & Esipov, V. F. 1970 Astrofizika, 6, 39

Bade, N., Fink, H. H., Engels, D., Voges, W., Hagen, H.-J., Wisotzki, L., & Reimers, D. 1995, ApJS, 110, 469

Barcons, X., Franceschini, A., De Zotti, G., Danese, L., and Miyaji, T. 1995, ApJ, 455, 480

Barger, A.J., Cowie, L.L., Bautz, M.W., Brandt, W.N., Garmire, G.P., Hornschemeier, A.E., Ivison, R.J., & Owen, F.N. 2001, AJ, 122, 2177

Barger, A.J., et al. 2002, AJ, 124, 1839

Barkhouse, W.A., & Hall, P.B. 2001, AJ, 121, 2843

Becker, R. H., White, R. L., & Helfand, D. J. 1995, ApJ, 450, 559

Braccesi, A., Lynds, R., & Sandage, A. 1968, ApJ, 152, 105

Brandt, W.N., Mathur, S., & Elvis, M. 1997, MNRAS, 285, L25

Brandt, W.N., et al. 2001, AJ, 122, 2810

Burke, B.E., Mountain, R.W., Harrison, D.C., Bautz, M.W., Doty, J.P., Ricker, G.R., & Daniels, P.J. 1991, IEEE-ED, 38, 1069

Cardelli, J.A., Clayton, G.C., & Mathis, J.S. 1989, ApJ, 345, 245

Condon, J.J., Cotton, W.D., Greisen, E.W., Yin, Q.F., Perley, R.A., Taylor, G.B., & Broderick, J.J. 1998, AJ, 115, 1693

Crawford, C.S., et al. 1995, MNRAS, 274, 75

Croom, S. M., Smith, R. J., Boyle, B. J., Shanks, T., Loaring, N. S., Miller, L., & Lewis, I. J. 2001, MNRAS, 322, L29

Comastri, A., Setti, G., Zamorani, G., & Hasinger, G. 1995, A&A, 296, 1

Della Ceca, R., Zamorani, G., Maccacaro, T., Wolter, A., Griffiths, R., Stocke, J.T., & Setti, G. 1994, ApJ, 430, 533

Dickey, J.M., & Lockman, F.J. 1990, ARA&A, 28, 215

Elvis, M., et al. 1994, ApJS, 95, 1

Fiore, F., et al. 1999, MNRAS, 306, L55

Franceschini, A., Braito, V., & Fadda, D. 2002, astro-ph/0205529

Giacconi, R., et al. 2002, ApJS, 139, 369

Gilli, R., Salvati, M., Hasinger, G. 2001, A&A, 366, 407

Giommi, P., et al. 1991, ApJ, 378, 77

Hartwick, F.D.A., & Schade, D. 1990, ARA&A, 28, 437

Hooper, E.J., Impey, C.D., Foltz, C.B., & Hewett, P.C. 1996, ApJ, 473, 746

Hornschemeier, A.E., et al. 2001, ApJ, 554, 742

Inoue, H., 1985, Space Science Reviews, 40, 317

Ishisaki, Y., Ueda, Y., Yamashita, A., Ohashi, T., Lehmann, I., & Hasinger, G. 2001, PASJ, 53, 445

Iwasawa, K., Fabian, A.C., Brandt, W.N., Crawford, C.S., & Almaini, O. 1997, MNRAS, 291, L17

Kashikawa N., et al. 2002, PASJ, 54, 819

Kleinmann, S.G., et al. 1994, Ap&SS, 217, 11

Kotilainen J.K., Ward, M.J., & Boisson, C., et al. 1992, MNRAS, 256, 125

Kriss, G. A., & Canizares, C. R. 1982, ApJ, 261, 51

La Franca, F., et al. 2002, ApJ, 570, 100

Lawrence, A. 1991, MNRAS, 252, 586

Lewis, D. L., Macalpine, G. M., & Weedman, D. W. 1979, ApJ, 233, 787

Madgwick, D.S., et al. 2002, MNRAS, 333, 133

Mainieri, V., Bergeron, J., Rosati, P., Hasinger, G., & Lehmann, I. 2002, astro-ph/0202211

Maiolino, R., & Rieke, G.H. 1995, ApJ, 454, 95

Maiolino, R., et al. 2000, A&A, 355, l47

Maiolino, R., et al. 2001a, A&A, 365, 28

Maiolino, R., Marconi, A., & Oliva, E. 2001b, A&A, 365, 37

Marshall, H. L., Tananbaum, H., Huchra, J. P., Zamorani, G., Braccesi, A., & Zitelli, V. 1983, ApJ, 269, 42

Mason et al. 2000, MNRAS, 311, 456

McMahon, R.G., Irwin, M.J., & Hazard, C. 1992, Gemini Issue, 36, 1

Mulchaey, J.S., Koratkar, A., Ward, M.J., Wilson, A.S., Whittle, M., Antonucci, R.R.J., Kinney, A.L., Hurt, T. 1994, ApJ, 436, 586

Olsen, E.T. 1970, ApJ, 75, 764

Ohashi, T., et al. 1996, PASJ, 48, 157

Ohta, K., Yamada, T., Nakanishi, K., Ogasaka, Y., Kii, T., & Hayashida, K. 1996, ApJ, 458, L57

Piccinotti, G., Mushotzky, R. F., Boldt, E. A., Holt, S. S., Marshall, F. E., Serlemitsos, P. J., & Shafer, R.A. 1982, ApJ, 253, 485

Pickles, A.J. 1998, PASP, 110, 863

Predehl, P., & Schmitt, J.H.M.M. 1995, A&A, 293, 889

Rosati, P., et al. 2002, ApJ, 566, 667

Schmidt, M. 1974, ApJ, 193, 505

Smith, H.E., Spinrad, H., & Smith, E.O. 1976, PASP, 88, 621

Stern, D., et al. 2002, ApJ, 568, 71

Stocke, J.T., Morris, S.L., Gioia, I.M., Maccacaro, T., Schild, R., Wolter, A., Fleming, T.A., & Henry, J.P. 1991, ApJS, 76, 813

Strittmatter, P. A., Serkowski, K., Carswell, R., Stein, W. A., Merrill, K. M., & Burbidge, M. M. 1972, ApJ, 175, 7

Tresse, L., Rola, C., Hammer, F., Stasinska, G., Le Fevre, O., Lilly, S. J., & Crampton, D., 1996, MNRAS, 281, 847

Ueda, Y., et al. 1999a, ApJ, 518, 656

Ueda, T., Takahashi, T., Ohashi, T., & Makishima, K. 1999b, ApJ, 524, L11

Ueda, Y., Ishisaki, Y., Takahashi, T., Makishima, K., & Ohashi, T. 2001, ApJS, 133, 1 [Paper I]

Ueda, Y., Akiyama, M., Ohta, K., & Miyaji, T. 2003, ApJ, submitted

Veilleux, S., & Osterbrock, D.E. 1987, ApJS, 63, 295

Vikhlinin, A., McNamara, B. R., Forman, W., Jones, C., Quintana, H., & Hornstrup, A. 1998, ApJ, 502, 558

Voges, W., et al. 1999, A&A, 349, 389

Weedman, D. W. 1985, ApJ, 57, 523

White, N.E., Giommi, P., & Angelini, L. 1994, IAU Circ., 6100, 1

Wilkes, B.J., Wright, A.E., Jauncey, D.L., & Peterson, B.A. PASA, 1983, 5, 2

Wilkes, B.J., Schmidt, G.D., Cutri, R.M., Ghosh, H., Hines, D., Nelson, B., & Smith, P 2002, ApJ, 564, L65

Yasuda, N., et al. 2001, AJ, 122, 1104

Zamorani, G., Henry, J.P., Maccacaro, T., Tananbaum, H., Soltan, A., Avni, Y., Liebert, J., Stocke, J., Strittmatter, P.A., Weymann, R.J., Smith, M.G., & Condon, J.J. 1981, ApJ, 245, 357

This preprint was prepared with the AAS LaTeX macros v5.0.

Table 1: CANDIDATES OF OPTICAL COUNTERPARTS AND RESULTS OF THE IDENTIFICATIONS

Table 2: APPARENT PROPERTIES OF IDENTIFIED OBJECT

Table 3: ABSOLUTE PROPERTIES OF IDENTIFIED OBJECTS

Table 4: OPTICAL EMISSION LINE PROPERTIES OF IDENTIFIED OBJECTS

Fig. 1.— Left) $3' \times 3'$ finding charts centered on the positions of AMSSn sources. North is up and east is to the left. A large circle at the center of each finding chart represents the 90% error region of AMSSn source. (Only for 1AXG J000605+2031(NE01), the center of the finding chart is shifted.) Circles with radii of $10''$, $30''$, and $45''$ represent positions of *ROSAT* HRI, PSPC, and RASS sources, respectively. The triangles indicate positions of *Chandra* and *XMM-Newton* sources. The small and large squares indicate positions of FIRST and NVSS 1.4GHz radio sources, respectively. Middle) Close up view of the optical counterpart of each X-ray source is shown. The field of view is $15'' \times 15''$. Right) Optical spectrum of the identified object. The optical spectra are flux calibrated by standard star observation. The wavelengths of major emission and absorption lines are marked with vertical lines. The hatched area represents the wavelength affected by strong night sky lines or atmospheric absorptions.

Fig. 2.— Stacked surface number density distribution of NVSS 1.4 GHz radio sources centered on the 87 AMSSn hard X-ray selected source positions. The uncertainty is estimated by assuming Poisson statistics in each bin. There is an excess in the number density of radio sources within $\sim 1'$ of AMSSn hard X-ray selected sources.

Fig. 3.— Hβ broad-line width versus apparent photon index ($\Gamma_{\rm app}$) for AMSSn (open circles) and ALSS AGNs (open squares). There is no population of narrow-line Seyfert 1s which show a small Hβ line width (~ 1000 km^{-1}) and a large apparent photon index ($\Gamma_{\rm app} > 2$).

Fig. 4.— [N II]λ6583 to Hα narrow emission line ratio versus [O III]λ5007 to Hβ narrow emission line ratio diagram for narrow lines in the AMSSn objects. Identified narrow-line AGNs are indicated with filled squares. Narrow-line objects which are not identified with the X-ray sources, i.e. serendipitous objects, are marked with crosses. The open squares represent broad-line AGNs with strong narrow-lines in the AMSSn sample. The region occupied by Seyfert galaxies, LINERs, and HII-region like galaxies are shown with solid lines (Veilleux and Osterbrock 1987). All of the identified narrow-line AGNs lie in the region occupied by Seyfert galaxies.

Fig. 5.— Distribution of the ratio between the distance of optical counterpart to the X-ray source center and the estimated 90% error radius of the X-ray source. The distribution is consistent with the estimated 90% error radius.

Fig. 6.— $R-$band magnitude versus 2–10 keV hard X-ray flux distribution of hard X-ray selected objects. The AMSSn AGNs are plotted with open circles. Open squares and small dots indicate ALSS AGNs (AOY00) and *Beppo-SAX* objects (La Franca et al. 2002), respectively. Open triangles are *HEAO1* A2 AGNs (Piccinotti et al. 1982). Asterisks indicate

sample from *Chandra* surveys in CDFN (Brandt et al. 2001, Barger et al. 2002) and CDFS (Giacconi et al. 2002). Upper limits in the sample is indicated with filled triangles. Dashed lines represent the constant X-ray to optical flux ratios of $\log f_{2-10\mathrm{keV}}/f_R = +3$, $+2$, $+1$, 0, -1, -2, -3, and -4 from top to bottom. The 2–10 keV hard X-ray fluxes of AMSSn AGNs are determined from the count rates, the Γ_{app} of each source, and GIS instrument response. Galactic absorption is corrected.

Fig. 7.— Hard X-ray luminosity versus redshift for hard X-ray selected AGNs. Open circles and open squares are AMSSn and ALSS AGNs, respectively. Open triangles are *HEAO1* A2 samples. Asterisks represent sample from *Chandra* survey in CDFN (Brandt et al. 2001, Barger et al. 2002). The *ASCA* AGN sample is two orders of magnitude brighter than the *Chandra* objects at the same redshifts.

Fig. 8.— Apparent photon index in the 0.7–10 keV band versus redshift for AMSSn (open circles) and ALSS (open squares) AGNs. The uncertainties of the Γ_{app} determinations are typically 0.2 (0.5) for objects with $\Gamma_{\mathrm{app}} > 1$ (< 1). No broad Hβ AGNs are marked with large crosses. Small dots indicate objects with $\log f_{2-10\ \mathrm{keV}}/f_R > +1$. BL Lac objects are marked with large circles. The horizontal dashed line indicates the Γ_{app} of 1. The vertical dashed line marks the redshift of 0.6. The wavelength range of the Hβ line is observed only for objects below this redshift. The solid lines show the Γ_{app} of the intrinsic power-law continuum with Γ of 1.7 absorbed by $N_{\mathrm{H}} = 1 \times 10^{22}$ cm^{-2} (upper) and 1×10^{23} cm^{-2} (lower) at each redshift.

Fig. 9.— Distribution of apparent photon index (Γ_{app}) of the AMSSn (shaded) and ALSS AGNs (open). Both of the distributions peak at Γ_{app} of 1.5 to 2.

Fig. 10.— Estimated hydrogen column density versus absorption-corrected hard X-ray luminosity for the AMSSn (open circles) and ALSS AGNs (open squares) at $z < 0.6$ (a) and at $z > 0.6$ (b). AGNs with $\Gamma_{\mathrm{app}} > 1.7$ are plotted at $N_{\mathrm{H}} < 1 \times 10^{20}$ cm^{-2} with uncertainty of 0. In the panel (a), the AMSSn and ALSS no broad Hβ AGNs are marked with large crosses. In the panel (b), two AGNs without significant broad line, 1AXG J160118+0844(NO53) and 1AXG J233200+1945(NO18), are marked with large crosses. Small dots indicate the AGNs with a large optical to hard X-ray flux ratio ($\log f_{2-10\ \mathrm{keV}}/f_R > +1$). It should be noted that the upper envelopes of the hydrogen column density distributions represent the selection limit of the 2–10 keV selection.

Fig. 11.— $J - K_S$ color versus redshift for AMSSn (open circles) and ALSS AGNs (open squares). AGNs which are not detected in 2MASS survey are plotted below $J - K_S$ color of 0. AGNs with $N_{\mathrm{H}} > 1 \times 10^{22}$ cm^{-2} are marked with dots. The no broad Hβ AGNs are marked with large crosses. The small dots and crosses indicate color distribution of

optically-selected AGNs measured in 2MASS survey (Barkhouse and Hall 2001) and Seyfert galaxies (Kotilainen Ward and Boisson 1992), respectively. The $J - K_S$ color track of an elliptical galaxy is shown by the solid line. No evolution is considered in the color model. The reddest object in the AMSSn sample is 1AXG J121854+2957(NO07).

Fig. 12.— Luminosity distributions of $z < 0.6$ AMSSn, ALSS, and ADSL AGNs (open histogram) and AGNs with $N_{\mathrm{H}} > 10^{22}$ cm^{-2} in the sample (shaded histogram).

Fig. 13.— Luminosity distributions of $z < 0.6$ AMSSn, ALSS, and ADSL AGNs (open histogram) and no broad Hβ AGNs in the sample (shaded histogram).

Fig. 14.— Radio 1.4GHz luminosity versus V-band absolute magnitude for AMSSn (open circles) and ALSS (open squares) AGNs. Asterisks and crosses represent upper limits for AMSSn and ALSS AGNs which are not detected in the radio wavelength, respectively. Small dots indicate absorbed AGNs with $N_{\mathrm{H}} > 1 \times 10^{22}$ cm^{-2}. BL Lac objects are marked with large circles. The dashed line represents the radio-loud AGN criterion from Hooper et al. (1996)

Fig. 15.— Radio 1.4GHz luminosity versus absorption-corrected 2–10 keV luminosity for AMSSn (open circles) and ALSS (open squares) AGNs. Asterisks and crosses represent upper limits for AMSSn and ALSS AGNs which are not detected in the radio wavelength, respectively. Small dots indicate absorbed AGNs with $N_{\mathrm{H}} > 1 \times 10^{22}$ cm^{-2}. BL Lac objects are marked with large circles. Large squares indicate AGNs which are classified as radio-loud with radio to optical flux ratio ($\log R_{8.4\mathrm{GHz}} > 1$). The lower and upper dashed lines indicate typical hard X-ray to radio luminosity ratio of radio-loud and radio-quiet QSOs, respectively (Elvis et al. 1994). The proposed criterion for radio-loud AGNs is shown with the solid line.

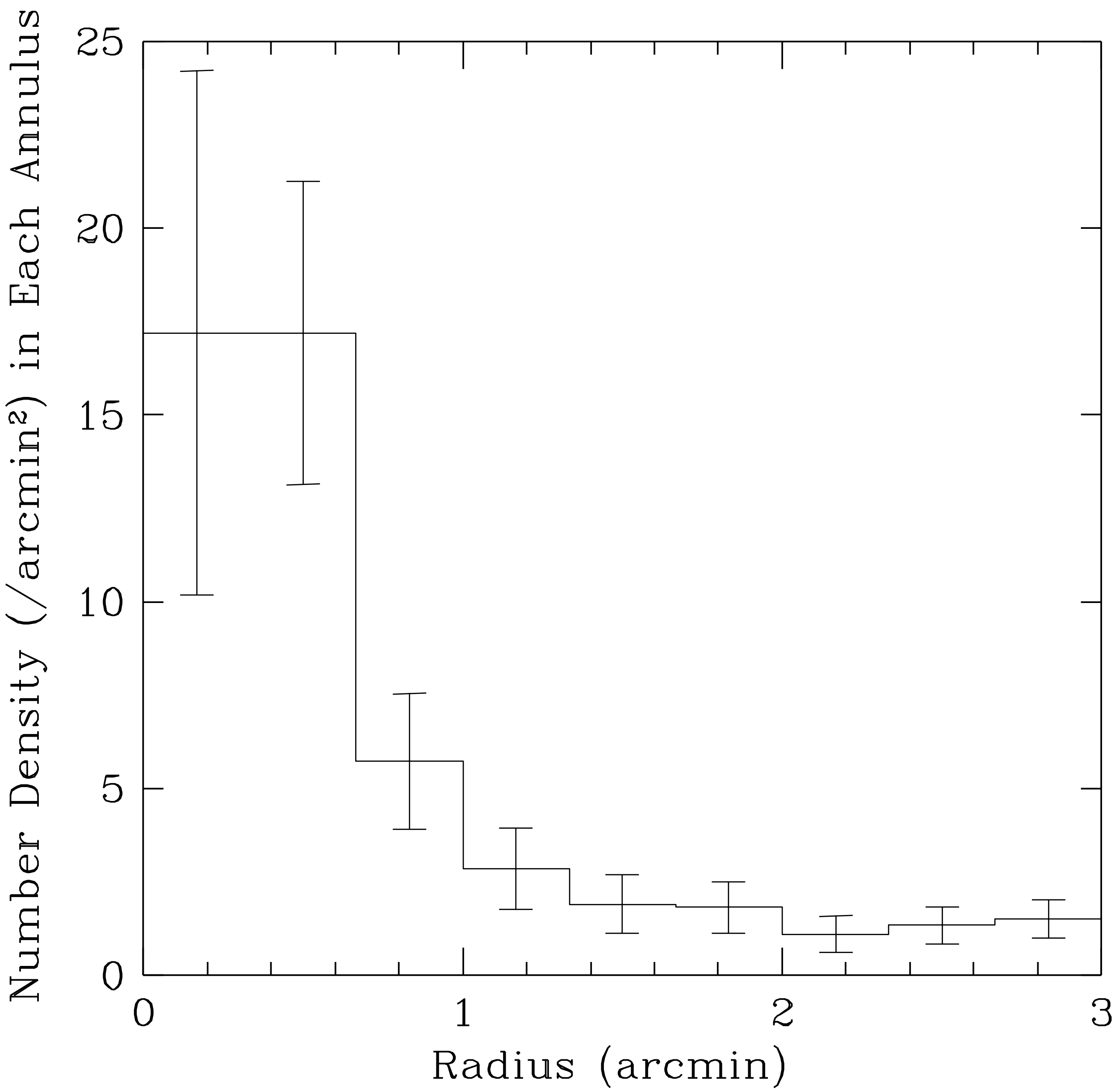

Number Density (/arcmin²) in Each Annulus
Radius (arcmin)
0
5
10
15
20
25
0
1
2
3

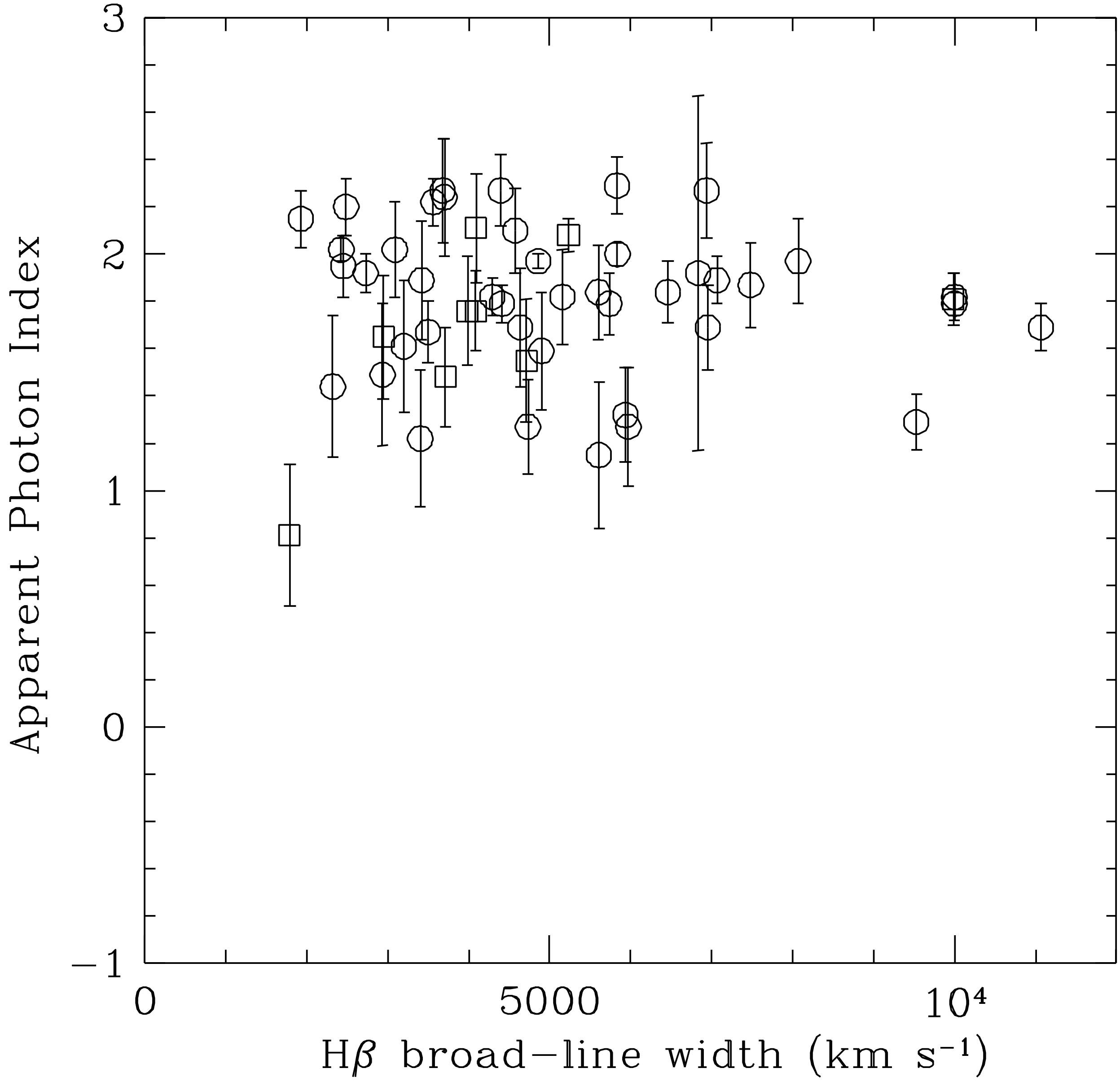
Apparent Photon Index
3
2
1
0
−1
0
5000
10^4
Hβ broad−line width (km s^{-1})

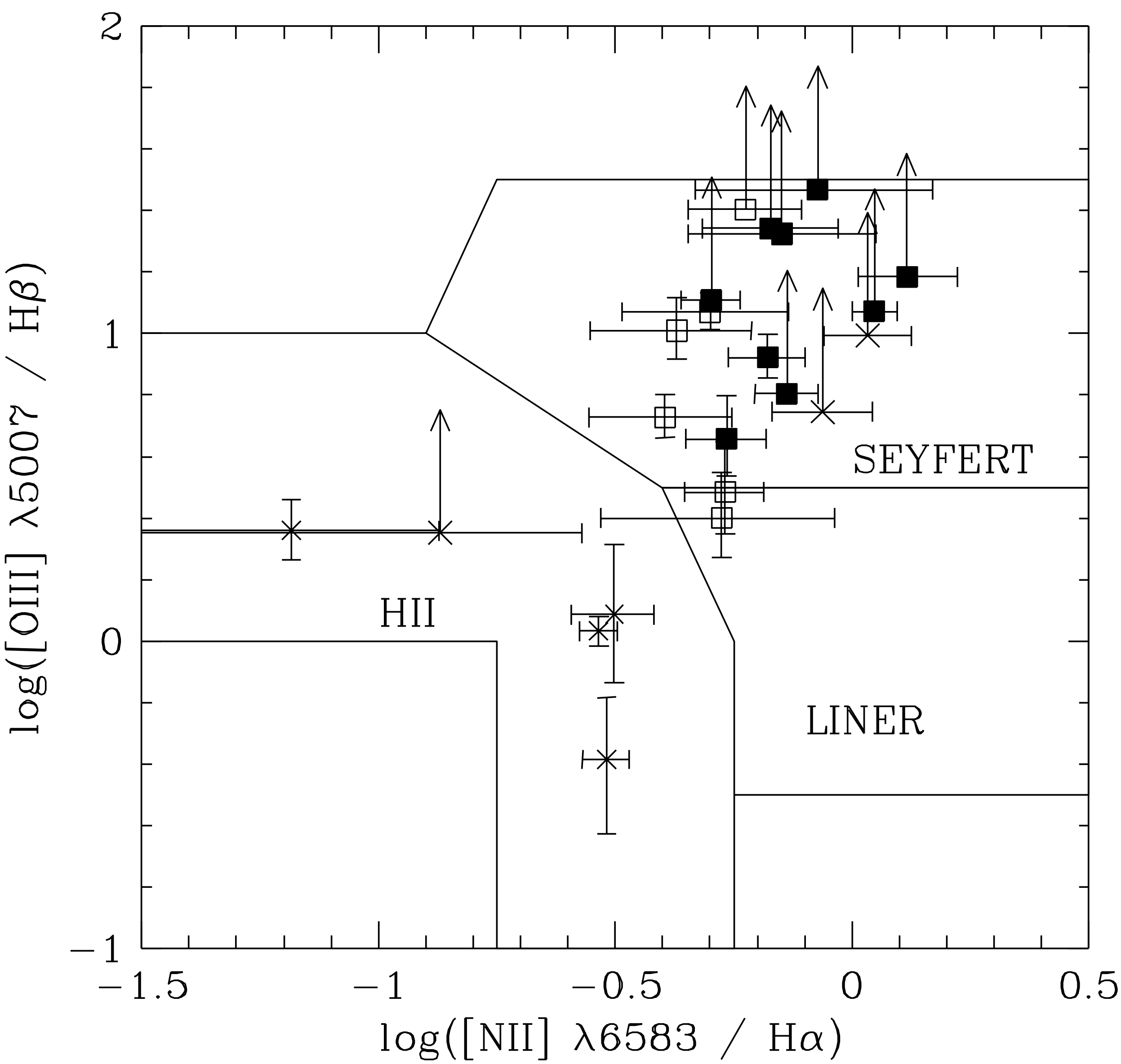

2
1
0
−1
−1.5
−1
−0.5
0
0.5
log([OIII] λ5007 / Hβ)
log([NII] λ6583 / Hα)
SEYFERT
HII
LINER

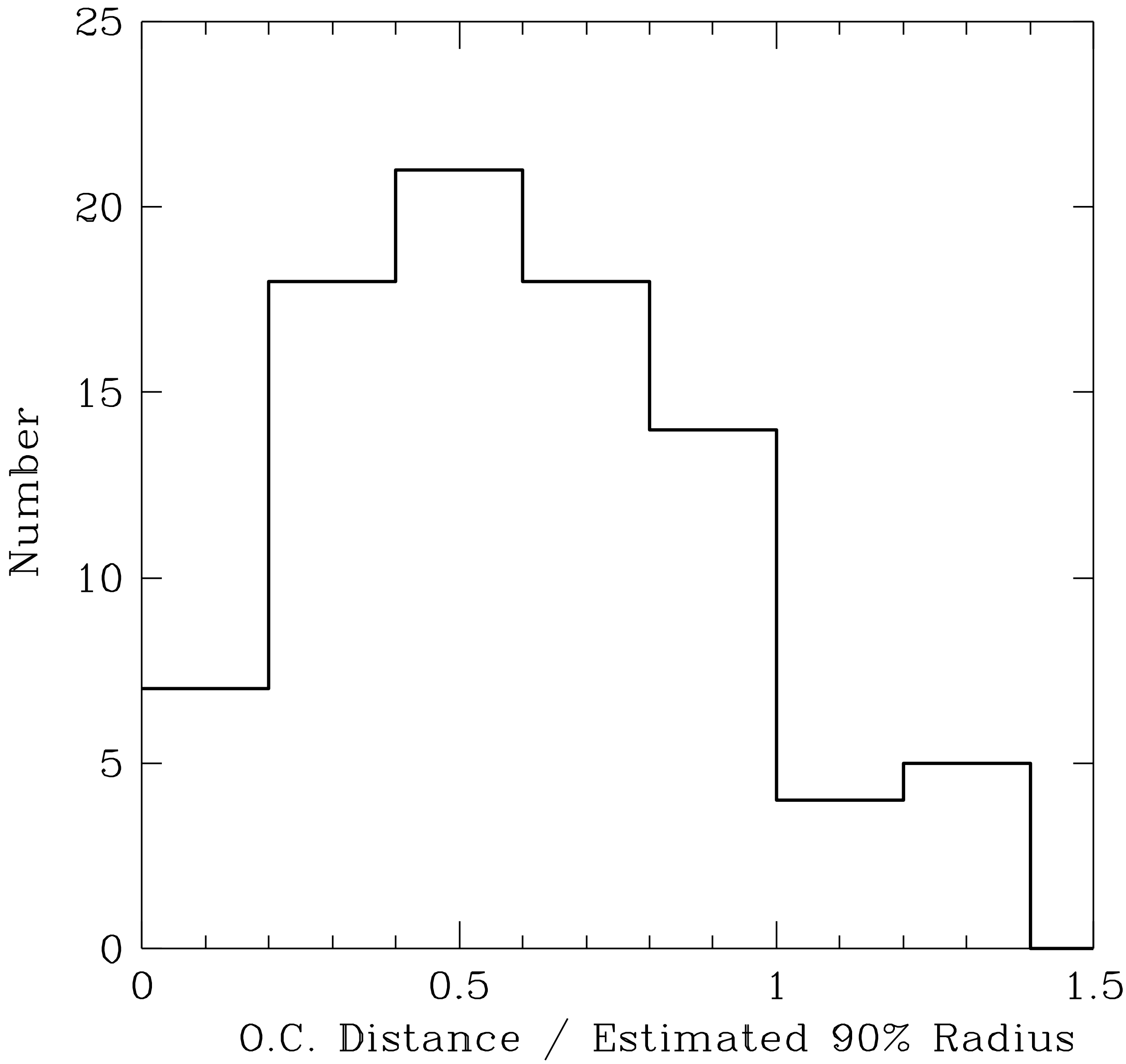

25
20
15
10
5
0
Number
0
0.5
1
1.5
O.C. Distance / Estimated 90% Radius

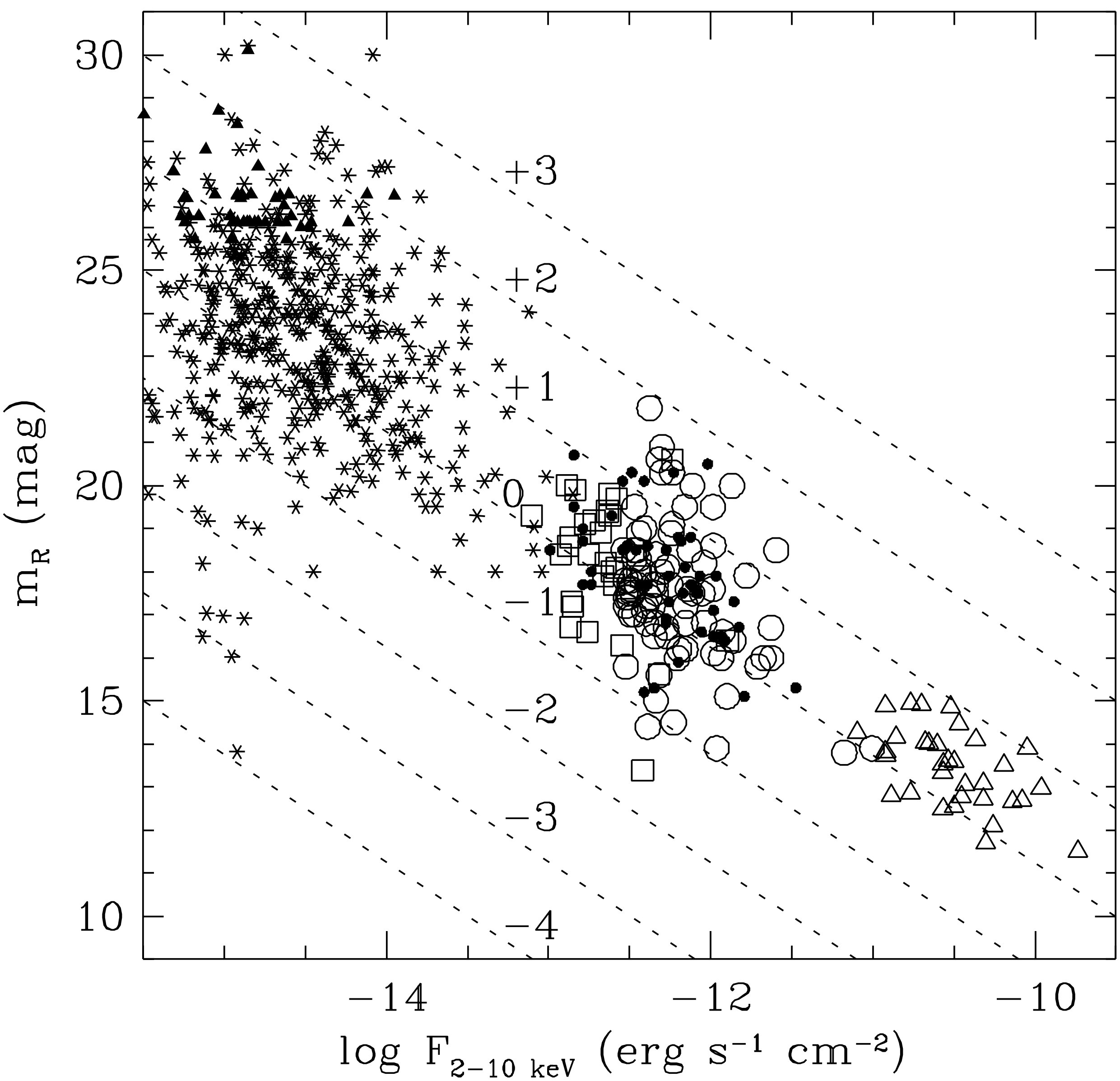
30
25
20
15
10
+3
+2
+1
0
−1
−2
−3
−4
−14
−12
−10
m_R (mag)
log $F_{2-10\ keV}$ (erg s^{-1} cm^{-2})

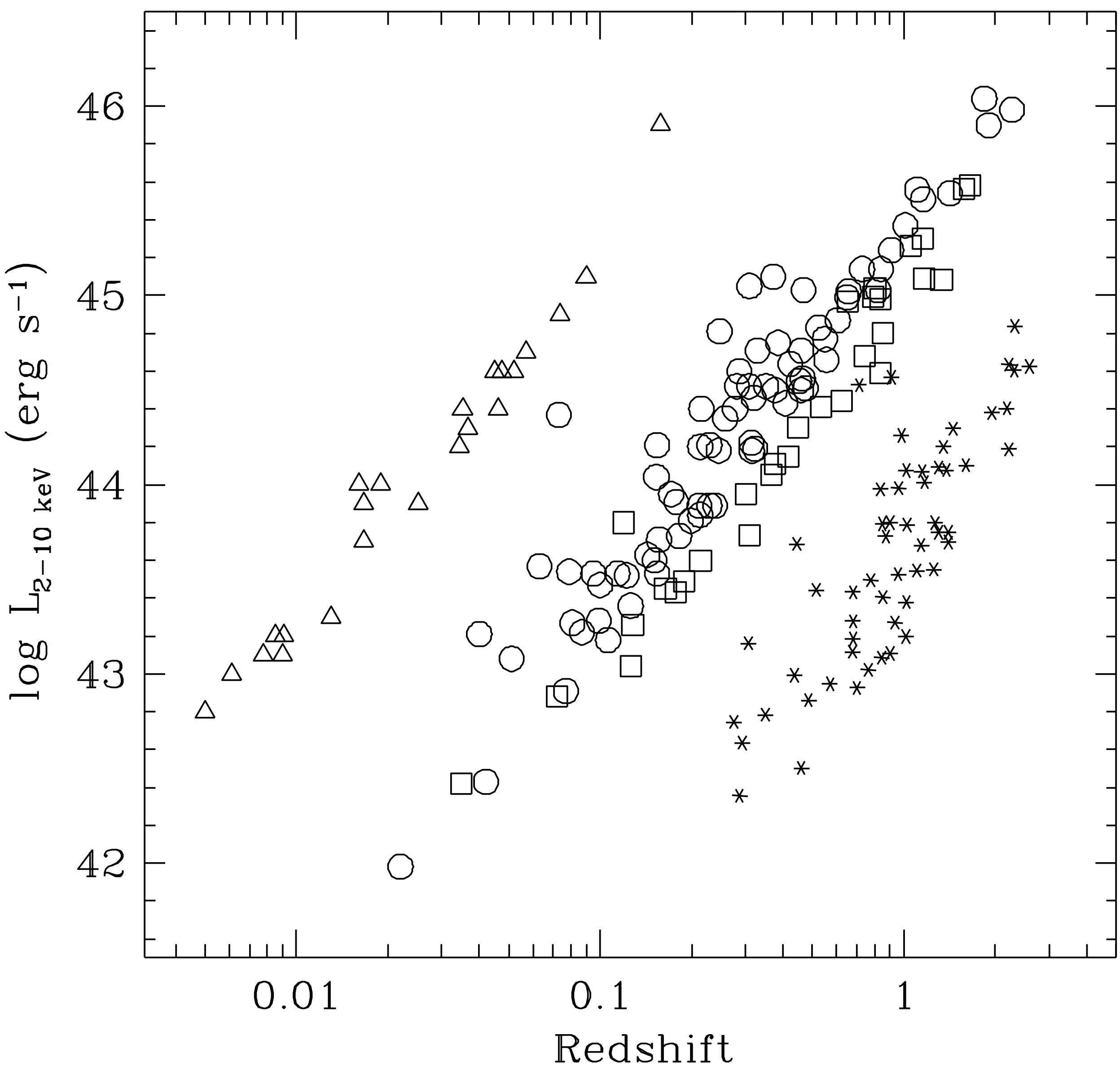
46
45
44
43
42
0.01
0.1
1
Redshift
log $L_{2-10\ keV}$ (erg s^{-1})

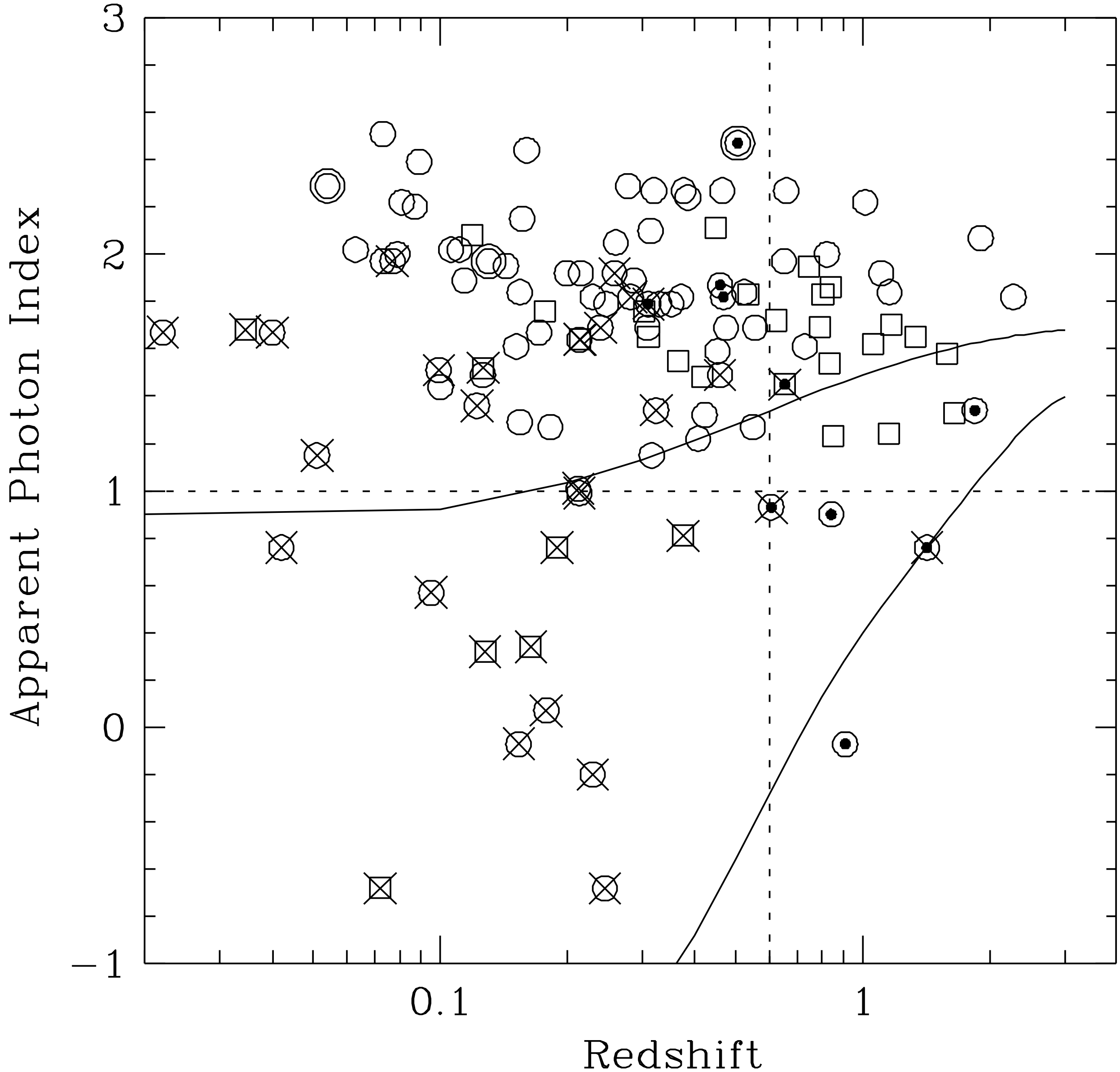

3
2
1
0
−1
Apparent Photon Index
0.1
1
Redshift

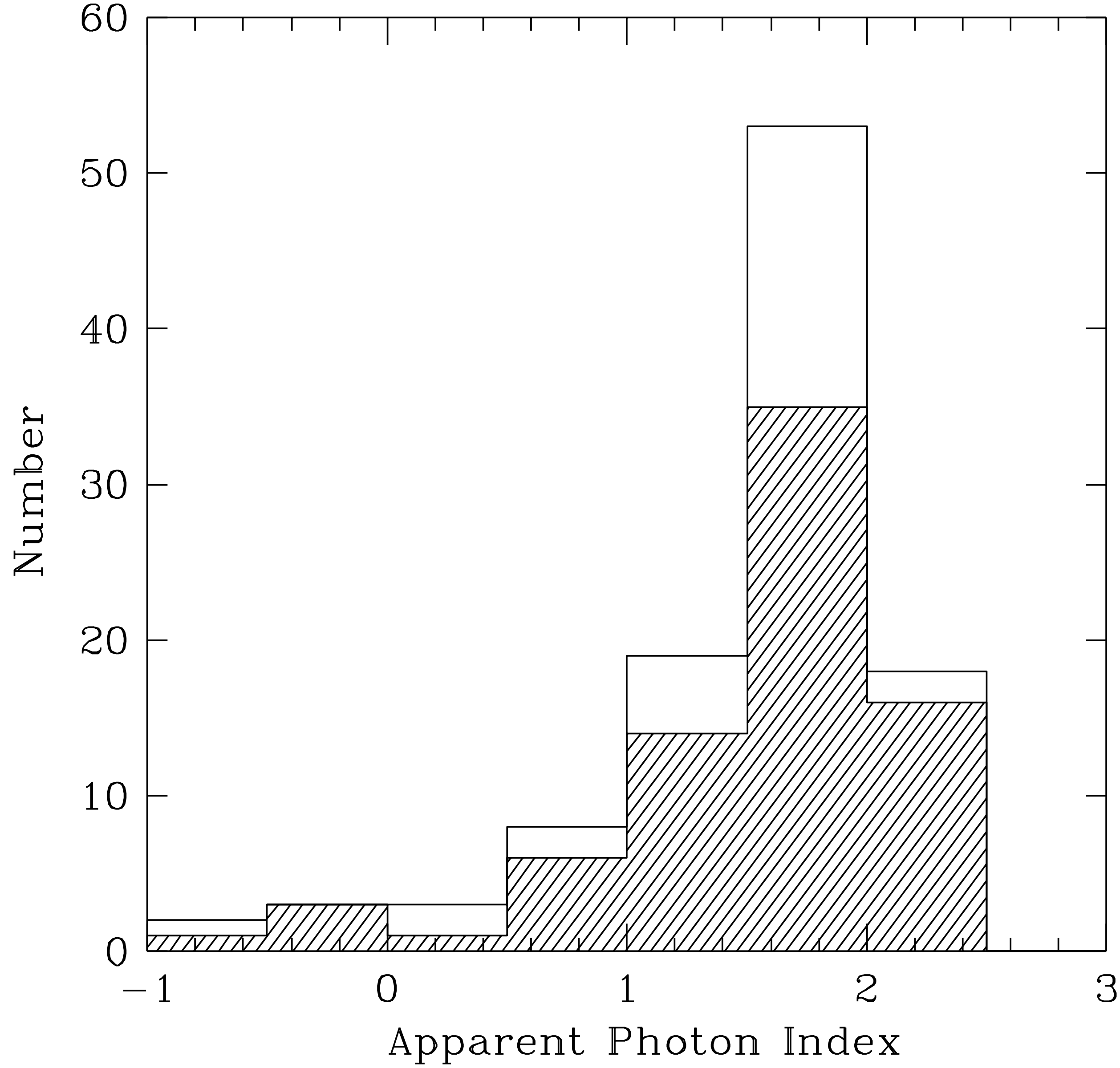

60
50
40
30
20
10
0
Number
−1
0
1
2
3
Apparent Photon Index

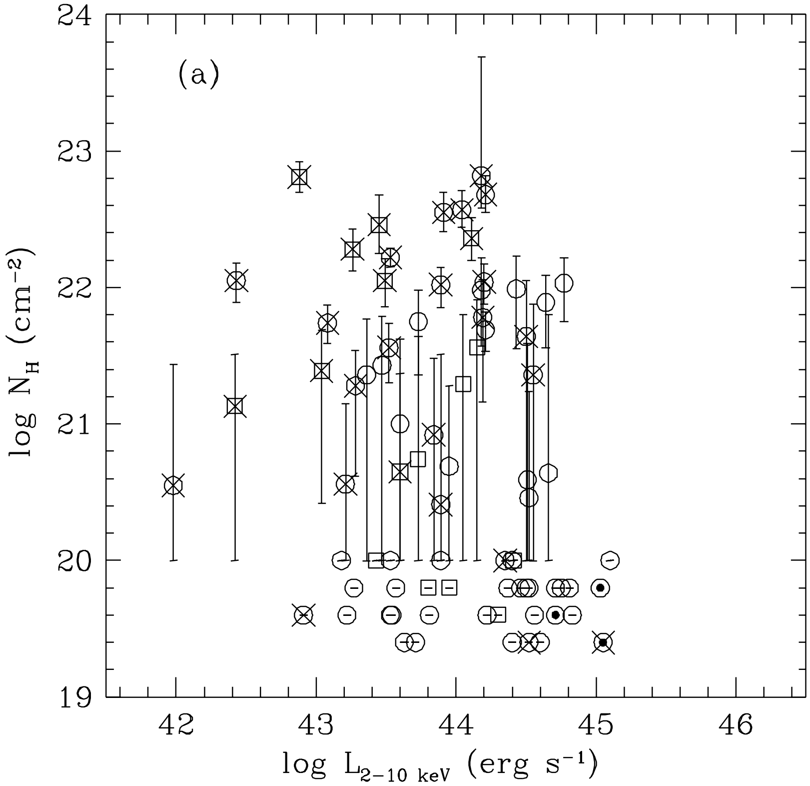

(a)
log N_H (cm^{-2})
log $L_{2-10\ keV}$ (erg s^{-1})
19
20
21
22
23
24
42
43
44
45
46

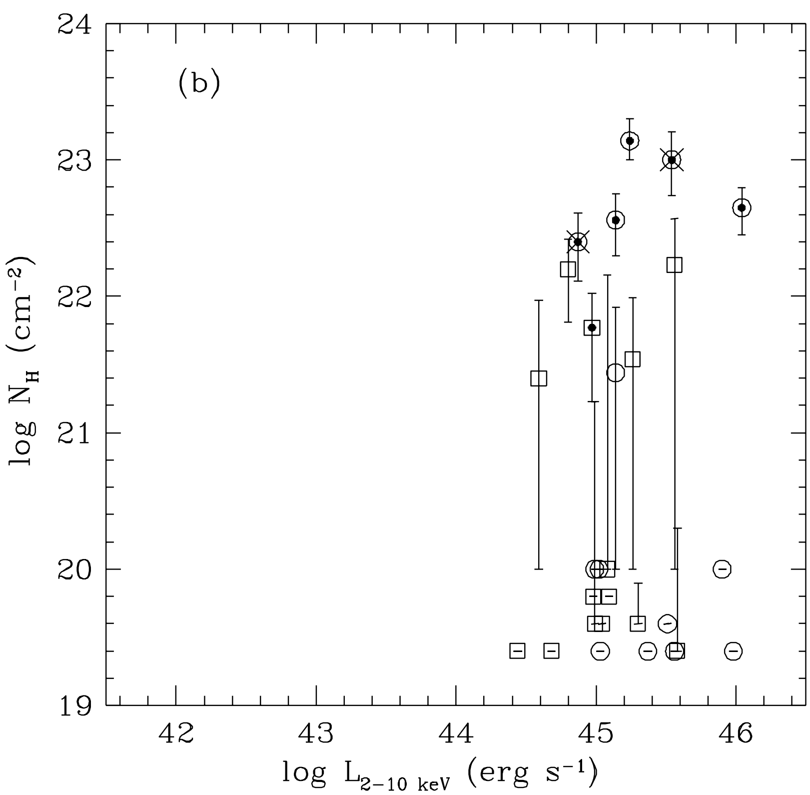

(b)
log N_H (cm^{-2})
log $L_{2-10\ keV}$ (erg s^{-1})
19
20
21
22
23
24
42
43
44
45
46

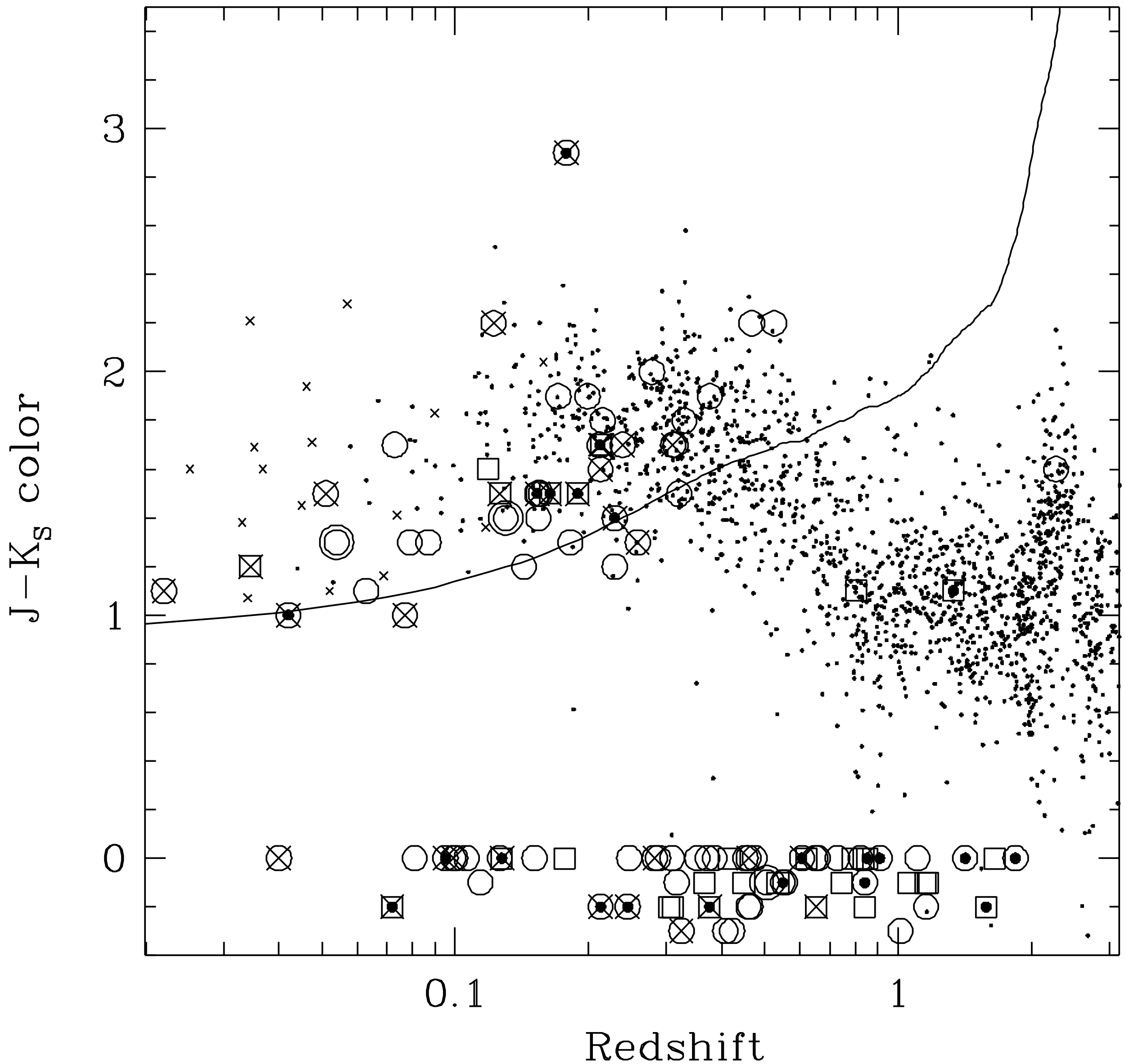
J−K$_S$ color
Redshift
0
1
2
3
0.1
1

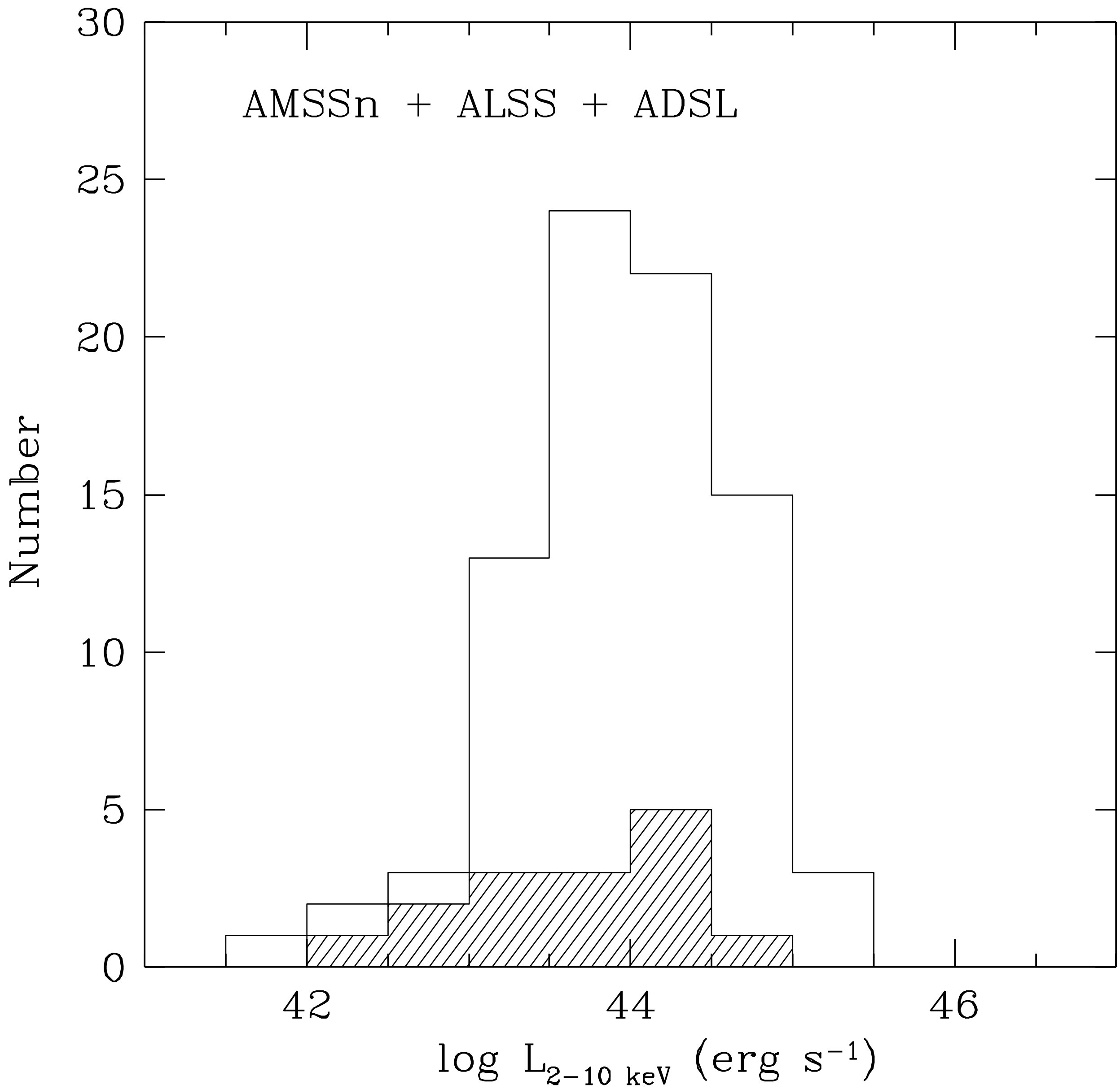

AMSSn + ALSS + ADSL
Number
0
5
10
15
20
25
30
42
44
46
log $L_{2-10\ keV}$ (erg s^{-1})

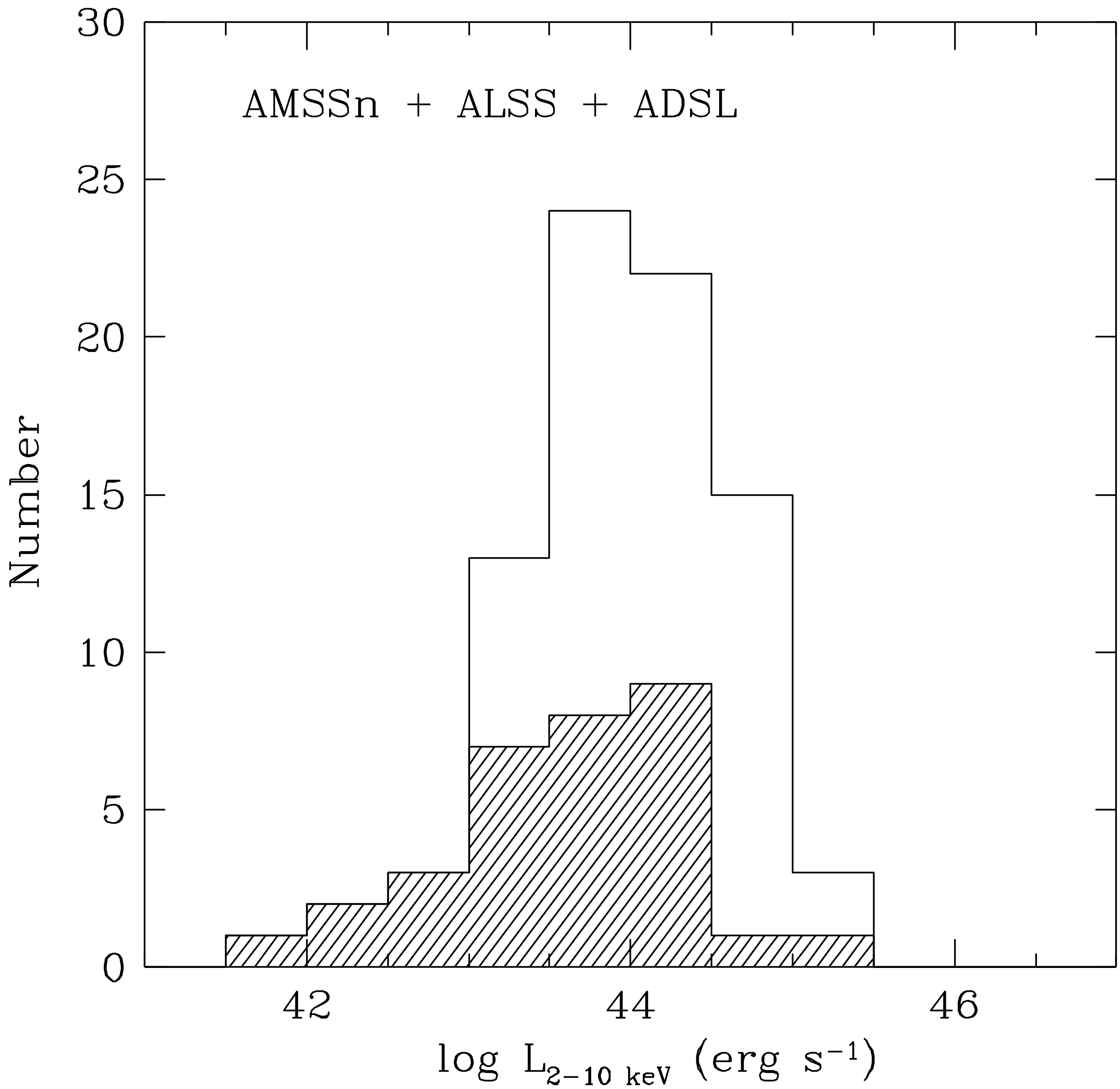

AMSSn + ALSS + ADSL
Number
0
5
10
15
20
25
30
42
44
46
log L2−10 keV (erg s−1)

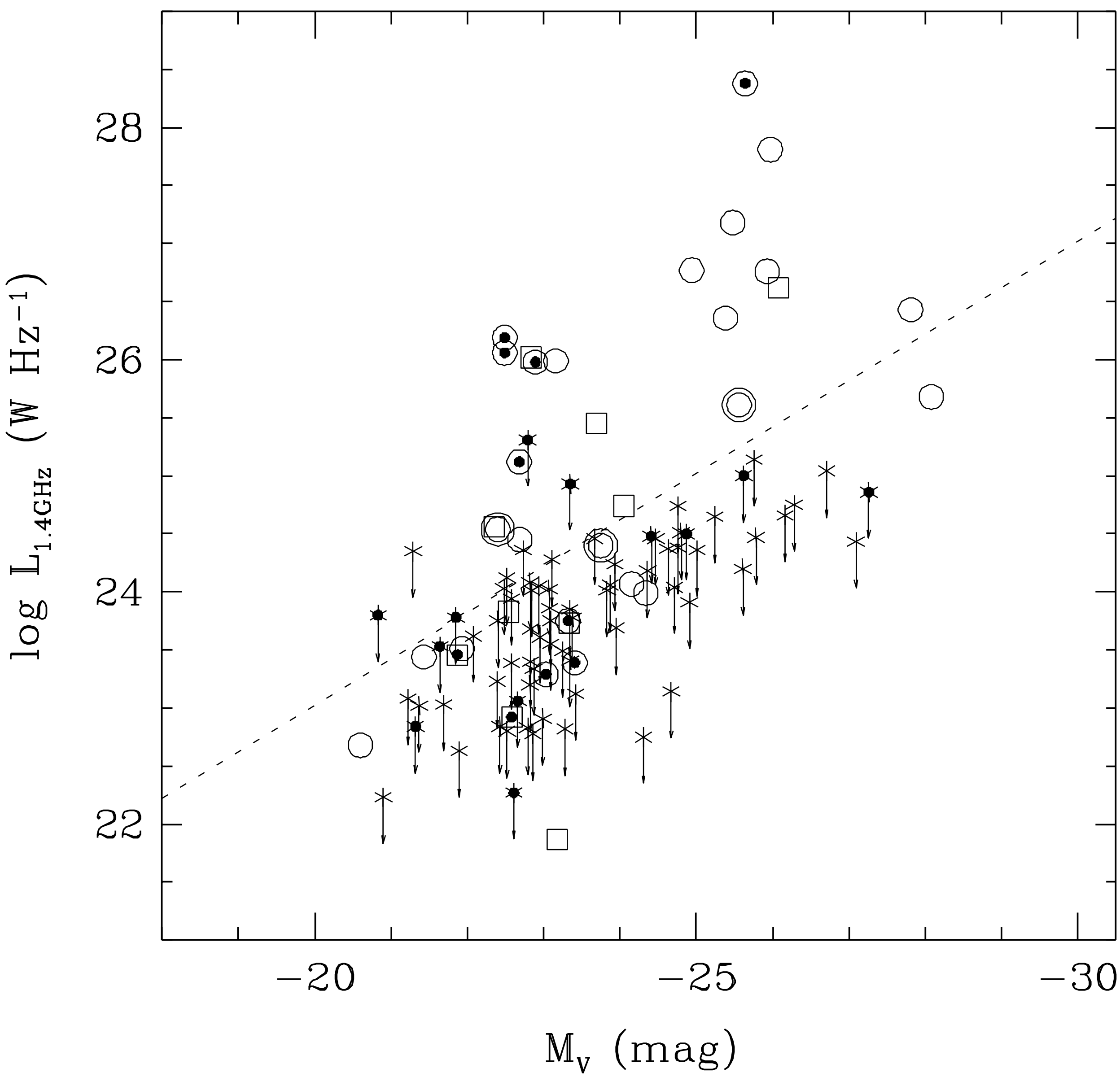
28
26
24
22
log $L_{1.4GHz}$ (W Hz^{-1})
−20
−25
−30
M_V (mag)

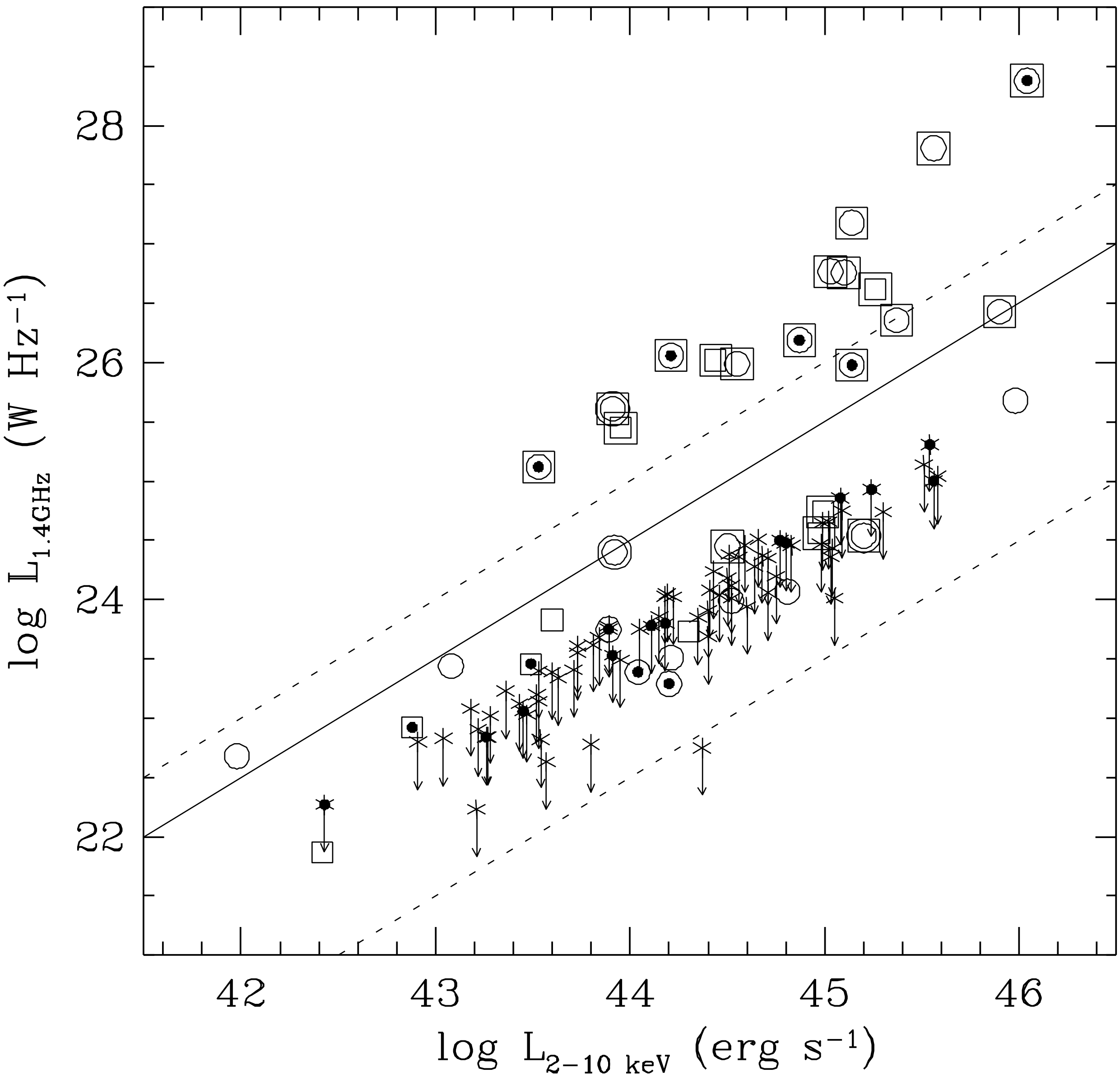

28
26
24
22
42
43
44
45
46
log $L_{1.4GHz}$ (W Hz^{-1})
log $L_{2-10\ keV}$ (erg s^{-1})